MEASUREMENTS OF AERODYNAMIC NOISE ON A FLAT PLATE IN SUPERSONIC FLOW

Thesis by

William S. Chen

In Partial Fulfillment of the Requirements

For the Degree of

Aeronautical Engineer

California Institute of Technology

Pasadena, California

1961

ACKNOWLEDGEMENT

Many persons have contributed to the success of this research program. Among those are Dr. Hans Liepmann and Dr. Antol Roshko, of the Guggenheim Aeronautical Laboratory, who provided assistance in the way of suggestions and criticisms. At the Jet Propulsion Laboratory, Dr. Alan Kistler of the Gas Dynamics section was a close associate who helped unselfishly with the wind tunnel testing and with the many technical problems connected with the program. In the Wind Tunnel section, the electronic instrumentation group under Dr. John Stallkamp developed and made available the equipment used in the tests. The mechanical instrumentation group was responsible for work on the flat plate and pressure transducer. Of particular value is the contribution of Mr. Samuel Wheeler; without whose skill the development of a first rate pressure transducer would have been next to impossible.

Thanks is also due Mrs. Gail Lambert, who helped with the computation of the results, and Miss Jeanne Kiley, who helped with the editing of the material in this manuscript.

ABSTRACT

Measurements of aerodynamic noise, in the form of pressure fluctuations in a turbulent boundary layer, were made on a smooth flat plate in the 12- and 20-in. supersonic wind tunnels at the Jet Propulsion Laboratory. The noise was measured with small piezoelectric pressure transducers (0.015-0.03 in. diameter) constructed of barium titanate crystals which were flush-mounted in the flat plate.

Spectral-energy distributions of the pressure fluctuations are obtained up to a frequency of 0.5 mc at freestream Mach numbers from 2.0 to 5.0, and Reynolds numbers based on boundary-layer-displacement thickness from 5×10^3 to 5×10^4. By grouping the test variables into the proper nondimensional forms and correcting for the finite transducer size, the energy spectra are found to be similar and uniquely related to both Mach number and Reynolds number. The total, or integrated, level of noise at the plate surface, in terms of root-mean-square values of the pressure fluctuations, is a constant equal to about 10 times the shear stress τ_w at the wall. The intensity, $\overline{p'^2}$, is directly proportional to the fourth power of the freestream Mach number.

Correlation measurements in time and in the streamwise direction in space show that the noise at the plate surface is convected downstream with a characteristic velocity equal to 75% of the freestream velocity. The correlation dies off rapidly with spacing between pickup points, and the convection velocity shows no dependence on either Mach number or Reynolds number.

TABLE OF CONTENTS

I. Introduction 1

II. Test Facility and Test Model 4

A. Flat Plate and Shock Mounting 5

B. Description of Barium Titanate Pressure Transducer 6

C. Calibration of the Pressure Transducer 7

III. Electronic Instrumentation 9

IV. Basic Measurements 10

A. Boundary Layer Velocity Profiles 10

B. Energy Spectrum 11

C. Space-Time Correlations 16

V. Results and Conclusions 17

Appendices

A. Spectral Measurements in Subsonic Flow 21

B. List of Electronic Equipment 23

C. Abbreviations of Manufacturers' Names 25

Figures 26

NOMENCLATURE

a_w	sound speed based on the adiabatic wall temperature
a_∞	sound speed in the freestream
$A(k_1)$	frequency attenuation of energy spectrum
$A_f(k_1)$	amplitude attenuation of energy spectrum
C_f	local skin friction coefficient
d	diameter of pressure transducer
f	frequency
J_1	Bessel function of the first order
k	$\lvert\vec{k}\rvert$ = vector sum of k_1 and k_3
k_1	wave number in streamwise direction of flow
k_3	wave number in transverse direction to flow
M_∞	freestream Mach number
$\tilde{p}$	root-mean-square pressure fluctuation
$\overline{p'^2}$	mean square pressure fluctuation
$P_o(f)$	true energy spectrum in streamwise direction as defined in Eq. (7)
p_t	stagnation pressure
p'_t	pitot-pressure
$P_3(k_3)$	energy spectrum in transverse direction to flow
q_∞	freestream dynamic pressure
r	radius of pressure transducer
Re	Reynolds number
$R\delta^*$	Reynolds number based on boundary-layer displacement thickness

NOMENCLATURE (Cont'd)

R_θ	Reynolds number based on boundary-layer momentum thickness
$R(\tau)$	correlation function as defined in Eq. (14)
t_t	stagnation temperature
V_c	convection velocity of noise
x	coordinate in streamwise direction, measured from leading edge of flat plate
y	coordinate normal to plane of flat plate
ΔP	shock strength or pressure jump
Δt	time interval between two measurements
ΔV	voltage rise corresponding to pressure jump
Δx	spacing between two measuring stations in the streamwise direction
δ^*	boundary-layer displacement thickness
θ	boundary-layer momentum thickness
$\phi_m(f)$	measured energy spectrum
ρ	density of fluid
τ	time of delay
τ_{opt}	time to optimum correlation
τ_w	shear stress at the wall

I. INTRODUCTION

The term "aerodynamic noise"--that is, any sound of an acoustical nature which is created from aerodynamic sources--includes sound fields produced by turbulent flows, such as those in jets, wakes, and boundary layers. Lighthill[1] was the first to present a theory of noise for the turbulent motion with explicit emphasis on the acoustical properties of such a motion. A number of theoretical and experimental studies have subsequently been published from this point of view. A general survey of the turbulence problem, of which aerodynamic noise is a part, may be found in a paper by Liepmann.[2]

The noise produced by the fluctuations in a turbulent boundary layer is of two types. If the boundary surface is perfectly rigid, the turbulent fluctuations will (1) radiate a sound field into the freestream, and (2) generate noise in the form of pressure and shear fluctuations at the solid surface. The first is known as the "far" field; the second, the "near" field. If the bounding surface is flexible, a third sound field is created by the coupling via the wall motion of the internal fluid to the

---

[1] M. J. Lighthill "On sound generated aerodynamically," Proc. Roy. Soc. (A), 211, 564 (1952).

[2] H. W. Liepmann, "Aspects of the turbulence problem," J. of Applied Math. and Physics, 3, (1952).

external flow field. This latter type of noise problem has been studied by Corcos and Liepmann,[3] and Weyers.[4]

The problem of noise in both "far" and "near" fields has been treated theoretically by many authors; e.g., Phillips,[5,6] Curle,[7] and Kraichnan[8]; experimental results are not as available. Measurements in the "far" field have been made by Mollo-Christensen and Narashimha,[9] using an air jet,[10] and by Laufer,[11] using the boundary layers on the

---

[3]G. M. Corcos and H. W. Liepmann, On the Transmission Through a Fuselage Wall of Boundary Layer Noise, Rept. No. SM-19570, Douglas Aircraft Company, Inc. December 1955.

[4]P. F. R. Weyers, On the Measurement of Acoustic Radiation Due to Wall Deformation by Turbulent Pipe Flow, Prog. Rept. No. 92. Guggenheim Laboratory, California Institute of Technology, Pasadena, California, April 27, 1957.

[5]Phillips, O. M., Surface Noise from a Plane Turbulent Boundary Layer, British A.R.C., Rept. No. 16, 963/FM 2099, (4 August 1954).

[6]Phillips, O. M., "On the Aerodynamic Sound From a Plane Turbulent Boundary Layer," Proc. Roy. Soc. (A) 234, 1198 (1955).

[7]Curle, N., "The Influence of Solid Boundaries Upon Aerodynamic Sound," Proc. Roy. Soc. (A), 231, 1187 (1955).

[8]R. H. Kraichnan, "Noise Transmission from Boundary Layer Pressure Fluctuations," J. Acoust. Soc. Am. 29, 65-80 (1957).

[9]E. Mollo-Christensen and R. Narashimha, Sound Emissions from Jets at High Subsonic Velocities, GALCIT report submitted to NASA March 1959.

[10]Jets are flows of boundary layer type and, therefore, are governed by the same equations of motion.

[11]J. Laufer, Aerodynamic Noise in Supersonic Wind Tunnels, Prog. Rept. No. 20-378. Jet Propulsion Laboratory, Pasadena, California, February 27, 1959.

wind tunnel walls. In the "near" field, measurements of the pressure fluctuations at subsonic speeds have been made by Willmarth[12, 13] (see App. A) and Harrison.[14]

The noise field increases sharply with increasing speed between the fluid medium and the solid surface. The noise produced by the turbulent boundary layer at supersonic and hypersonic speeds is of a particular interest. Laufer[11], for example, has found that the radiated sound intensity is proportional to M_∞^4 at supersonic speeds. As of this writing, no significant experimental data are available on either pressure fluctuations or shear fluctuations in the supersonic flow regime.

This report is concerned with the experimental research on the pressure-fluctuation noise in supersonic flow. The testing was performed in the supersonic wind tunnels at the Jet Propulsion Laboratory (JPL). A smooth flat plate was used as the test model. Measurements were made with small barium titanate piezoelectric crystals, 0.015 in. and 0.03 in. in diameter, which were flush-mounted in the flat plate.

---

[12] W. W. Willmarth, Wall Pressure Fluctuations in a Turbulent Boundary Layer, Natl. Advisory Comm. for Aeronaut., Tech. Note 4139 (March 1958).

[13] W. W. Willmarth, Space-Time Correlations and Spectra of Wall Pressure in a Turbulent Boundary Layer. NASA Memorandum 3-17-59W. (March 1959).

[14] M. Harrison, Pressure Fluctuations on the Wall Adjacent to a Turbulent Boundary Layer, Rept. 1260. David Taylor Model Basin, Maryland (December 1958).

The experimental data include measurements in the streamwise direction of (1) the spectral density of the pressure fluctuations, and (2) correlations of the spectra in time and at four points in space. An effort is made to develop the functional or similarity relationships between the measured quantities and the governing flow parameters. The primary objectives of this study are the determination of (1) the dependence of the energy distribution on Mach number and Reynolds number and (2) the convection characteristics of the fluctuation noise along the solid surface in the direction of flow.

II. TEST FACILITY AND TEST MODEL

The JPL 12- and 20-in. supersonic wind tunnels are of the continuous flow type (see Figs. 1 and 2). The nozzles of the tunnels are formed by a pair of flexible steel plates which are set to the desired nozzle contour by the method of continuous third derivatives.[15] Any Mach number from about 1.3 to 5.0 may be obtained in the 20-in. tunnel. The corresponding Mach range in the 12-in. tunnel is 1.3 to 4.0. By varying the supply pressure, the Reynolds number can be varied from about 15,000 to 500,000 per in. of characteristic length. The flow conditions

---

[15] N. Riise, Flexible Plate Nozzle Design for Two Dimensional Supersonic Wind Tunnels, Rpt. No. 20-74, Jet Propulsion Laboratory, Pasadena, California, June 9, 1954.

in both tunnels are quantitatively similar. A precise flow calibration[16] for a series of Mach numbers shows that the test-section air flow is uniform to within ±1% in both Mach number and static pressure and that the flow in the test rhombus is parallel to within ±0.1 deg. The turbulence level in the supply section is found to be 1%, or less, for all Mach numbers and Reynolds numbers.

A. Flat Plate and Shock Mounting

A flat plate is used as the test model to provide a smooth working surface for the experimental measurements. The plate is mounted in the 20-in. tunnel in the manner shown in Fig. 2. In order to isolate the plate from the tunnel vibrations, the plate is soft-mounted in the test section. The mounting bolts which support the plate are undercut to make room for a row of rubber O-rings. Also, rubber seals are inserted in the air gap between the plate and the tunnel door for the full length of the plate. In this way, contamination by flow across the gap is prevented, and the plate is completely isolated from metal-to-metal contact with the tunnel support. During testing, an electrical grounding circuit is used which automatically flashes a warning signal whenever the plate comes in contact with the tunnel door. This same system is used to indicate grounding between pitot probe and plate in the boundary-layer velocity-profile measurements.

---

[16] R. H. Steinbacher, Calibration of a Continuous Third-Derivative Nozzle in the 20-in. Supersonic Wind Tunnel, Jet Propulsion Laboratory.

The leading edge of the plate is equipped with a row of small orifices through which a small amount of air can be emitted to trip the boundary layer. The air-trip may be shut off at any time during the test, thus permitting periodic comparison with laminar flow conditions. Circular cutouts, which accommodate the 4-in. diameter inserts containing pressure transducers and other instrumentation, are made along the centerline of the plate, at stations 5.5, 13, and 24 in. from the leading edge. Thus, testing is possible over a wide range of boundary-layer thicknesses.

B. Description of Barium Titanate Pressure Transducer

In the present transducer design, small discs of polarized barium titanate crystals are carefully ground to size on a fine-grained diamond wheel. The smallest crystals made are of 0.015 in. diameter and 0.02 in. thickness. Some larger crystals, 0.03 in. diameter, were constructed for use in determining the effect of transducer size on the spectrum measurements. The disc sizes chosen are governed by a compromise for a pickup which would measure the pressure at a point and, at the same time, provide an adequate capacity and sensitivity. In practice, the criterion for a point measurement is that the diameter of the surface of the crystal is small as compared to the characteristic dimension of the flow, in this instance the boundary-layer displacement thickness. In other words,

$$d/\delta^* < 1 \qquad (1)$$

The amount of the amplitude and frequency attenuation of the measured signal is related to this ratio, which, for the present test, ranges from 0.1 to 0.5.

The pressure transducer is flush-mounted in the plate insert (Fig. 3) to minimize flow disturbances. A detail of the design and construction of the transducer is shown in Fig. 4. A soft rubber matrix[17] is used to isolate the crystal from possible transverse or shear loading and to shock-mount the transducer away from the flat plate. All cavities are filled with an epoxy resin[18] to prevent the occurrence of resonating columns of air (so-called Helmholtz resonators). This relatively intricate system is necessary to prevent the large amounts of extraneous signals in the test environment from reaching the crystal.

One or more crystals may be mounted on the same lead backing; usually, three crystals are placed together and diametrically spaced 0.25-in. apart on the transducer. For the correlation measurements, each of the crystals is of the same diameter; for measuring the effect of size, the crystals are of varying diameters.

C. Calibration of the Pressure Transducer

Initially, the pressure transducers are checked qualitatively with a small low-pressure air jet for uniformity of response to a randomly fluctuating type of input signal.

---

[17] Light-Bodied Permlastic, Kerr Mfg. Co., Detroit, Mich.

[18] A2 Adhesive, Armstrong Products Co., Warsaw, Ind.

A more precise calibration is made with a low-pressure shock tube. The shock tube and calibration instrumentation are shown in Fig. 5. The pressure transducer and plate-insert combination is flush mounted on the side of the tube. The shocks are produced by slowly increasing the pressure in the driving chamber until the diaphragm bursts. The desired low-pressure shock is obtained by using commercially available thin (1 mil) latex rubber[19] and aluminum foil for the diaphragm material.

The shock strength is determined by measuring the shock speed and using the normal shock relationship for a perfect gas. The shock speed is measured by identical barium titanate crystals spaced a known distance apart. Passage of the shock is sensed by these crystals in the form of instantaneous outputs which are used to start and stop the electronic timer. The average velocity over the two stations is then equal to $\Delta x/\Delta t$. A third barium titanate crystal is used to trigger the oscilloscope sweep, which is so adjusted time-wise that the transducer voltage output corresponding to the step loading from the shock wave is recorded on the scope screen.

A sample record of the transducer response is shown in Fig. 6a. The low-frequency oscillation of about 300 cps is the mechanical resonant frequency of the lead weight and soft-mounting system. The high-frequency oscillations ($\sim$1 Mc) near the step appear to differ from transducer to

---

[19] Youngs Rubber Corp., Trenton, N. J.

transducer and are believed to depend upon the slight variations in the mounting of the crystals on the lead backing of the individual transducers. The sensitivity calibrations for two crystals of different size are presented in Fig. 6b. The difference in sensitivity between crystals is the result of partial depolarization from the grinding process. The extent of this depolarization is dependent on crystal size.

III. ELECTRONIC INSTRUMENTATION

For the spectral measurements of the pressure fluctuations, the equipment is connected as shown in Fig. 7. Signals below 10 kc are filtered in the cathode follower to prevent extraneous low-frequency inputs from penetrating the electronic system. The remaining signal, which is measured to a frequency of 500 kc, is amplified by a wide-band amplifier to give approximately 1 volt of input to the wave analyzer. The gain in the analyzer is, in turn, adjusted to give an output to the thermocouple of sufficient amplitude to produce a full scale trace on the plotter.

For the correlation measurements, the equipment is connected as shown in Fig. 8. The two channels have identical cathode followers and amplifiers. The signal from the upstream transducer is delayed with a variable time-delay unit before subtraction from the downstream signal. The resultant signal is squared by a vacuum thermocouple and indicated on a potentiometer readout. The accuracy of the measurements is dependent on the phase relationship between the two channels and on the response characteristics of the time delay. A comparison of the

phase relationship shows that the two channels are within ±8 deg of each other from 20 to 100,000 cycles. However, superimposed on this relationship is the response and phase shift introduced by the time delay, which is by no means negligible.

Calibration of the time delay is made by measuring the autocorrelation of sine-wave inputs. The calibration is also tested by feeding into it a random noise signal with a known cutoff characteristic. The calculated and measured values of the autocorrelation with a random signal are shown in Fig. 9.

The electronic equipment used in the experiments is listed in App. B. Manufacturers of the equipment are identified in App. C.

IV. BASIC MEASUREMENTS

A. Boundary-Layer Velocity Profiles

The boundary layer is tripped by the bleeding of air through a row of small holes near the leading edge of the flat plate. The velocity profile is obtained by driving the pitot traverse toward the plate; a grounding circuit is used to indicate metal-to-metal contact between the probe and the plate. Typical traces of pitot data are presented in Fig. 10 for the three measuring stations in the axial direction. The corresponding profiles for determination of displacement and momentum thickness are shown in Fig. 11. As the thickness parameters are used to reduce the spectrum measurements to nondimensional form, the pitot traverse is

usually made immediately before or after each associated spectrum measurement to minimize changes in the basic flow conditions between the two types of data.

B. Energy Spectrum

Figure 12 is a typical data plot of the energy spectrum showing the amplitude distribution with frequency. The signal with a laminar boundary layer is seen to be quite small as compared with the turbulent case.

Three types of corrections are applied to the data: the first accounts for characteristics of the electronic equipment; the second corrects for the frequency attenuation of the measured signal due to the finite size of the pressure transducer; the third corrects the amplitude of the signal for attenuation in the direction transverse to that of the flow.

A general relationship has been worked out by Corcos[20] to correct for measurements with a transducer of finite size. The relationship is based on the assumptions that the turbulent pressure field is

1. a stationary random function; i. e., independent of time,
2. homogeneous (although not isotropic) in the plane of the vector wave number $\vec{k} = \vec{k}_1 + \vec{k}_3$.
3. convected downstream with a characteristic velocity relative to the freestream flow; i. e., in a "frozen" pattern.

[20]G. M. Corcos, et al, On the Measurement of Turbulent Pressure Fluctuations with a Transducer of Finite Size, Ser. 82, Issue 12. Institute of Engineering Research, University of California, Berkeley (1959).

The equation is

$$\phi_m(f) = P_0(f) \int_0^\infty \frac{J_1^2(kr)}{k^2r^2} \cdot P_3(k_3)\, dk_3 \qquad (2)$$

where

$\phi_m(f)$ = measured spectrum in direction of flow

$P_0(f)$ = true spectrum

$P_3(k_3)$ = spectrum in direction transverse to flow

$$k = |\vec{k}| = (k_1^2 + k_3^2)^{1/2}$$

$$k_1 = \frac{2\pi}{\lambda_1} = \frac{2\pi f}{V_c}$$

For the transducers used in this test, $k_1 < 2$ or 3. In this case, the Bessel function can be approximated[21] by

$$\frac{J_1^2(kr)}{k^2r^2} \simeq \frac{J_1^2(k_1r)}{k_1^2r^2} \cdot \frac{J_1^2(k_3r)}{k_3^2r^2} \qquad (3)[22]$$

The result is

$$\phi_m(f) = P_0(f) \frac{J_1^2(k_1r)}{k_1^2r^2} \int_0^\infty \frac{J_1^2(k_3)}{k_3^2r^2} P_3(k_3)\, dk_3 \qquad (4)$$

---

[21] The author is indebted to Dr. A. L. Kistler, JPL, for this suggestion.

[22] An error of about 6 to 7% is introduced by this approximation.

The term

$$J_1^2(k_1 r)/k_1^2 r^2 \equiv A_f(k_1) \tag{5}$$

corresponds to a frequency attenuation in the measured spectrum $\phi_m(f)$. The terms under the integral sign are independent of k_1, which means that the integral itself corresponds to an attenuation in the amplitude of $\phi_m(f)$ only. Unfortunately, not enough is known about $P_3(k_3)$, especially in supersonic flow, to permit explicit evaluation of the integral in the k_3 direction. The simplest assumption which can be made is that of two-dimensional isotropic turbulence in the plane of the flat plate. The integral then reduces to a multiplicative factor equal to

$$\int_0^\infty \frac{J_1^2(k_3)}{k_3^2 r^2} P_3(k_3) dk_3 = \frac{\displaystyle\int_0^\infty \frac{\phi_m(f)}{J_1^2(k_1 r)/k_1^2 r^2} df}{\displaystyle\int_0^\infty \phi_m(f)\, df} \equiv A(k_1) \tag{6}$$

and the general equation (Eq. 2) reduces to

$$\phi_m(f) = P_0(f) \cdot A_f(k_1) \cdot A(k_1) \tag{7}$$

A typical spectrum, Fig. 13, shows the relative magnitudes of the frequency and amplitude corrections on the measured spectrum. The frequency attenuation $A_f(k_1)$ is compared in Fig. 14 with the ratios of measured values of attenuation between transducers of two different sizes.

The measured values follow the general shape of the Bessel function, but, at the same time, exhibit a definite dependence on the Reynolds number. The amplitude attenuation $A(k_1)$ is shown in Fig. 15 to depend on Mach number and Reynolds number, as well as on transducer size. The decrease in attenuation with Mach number is the result of thickening of the boundary layer at the higher Mach numbers.

If it is assumed, as suggested by Liepmann,[23] that the mean square value of the fluctuating pressure is proportional to the square of the freestream dynamic pressure for fixed values of Mach number and Reynolds number, then

$$\frac{\overline{p'^2}}{q_\infty^2} = \int_0^\infty \frac{P_0(f)}{q_\infty^2}\, df = F(M_\infty, \mathrm{Re}) \tag{8}$$

Introducing the reduced frequency $f\delta^*/U_\infty$, this becomes

$$\int_0^\infty \frac{P_0(f\delta^*/U_\infty)}{q_\infty^2} \frac{U_\infty}{\delta^*}\, d\left(\frac{f\delta^*}{U_\infty}\right) = F(M_\infty, R_{\delta^*}) \tag{9}$$

---

[23] H. W. Liepmann, Parameters for Use in Buffeting Flight Tests, Report No. SM-14631, Douglas Aircraft Co., Inc., January 3, 1953.

Examining the integrand, it can be concluded that

$$\frac{P_0(f\delta^*/U_\infty)}{q_\infty^2}\,\frac{U_\infty}{\delta^*} = G\left(\frac{f\delta^*}{U_\infty},\ M_\infty,\ R_{\delta^*}\right) \tag{10}$$

An alternative, and perhaps more appropriate approach, is to base the pressure fluctuations on the shear stress at the wall.[24] In this case,

$$\frac{\overline{p'^2}}{\tau_w^2} = \int_0^\infty \frac{P_0(f)}{\tau_w^2}\,df = F(M_\infty,\ Re) \tag{11}$$

Introducing the reduced frequency based on momentum thickness, this becomes

$$\int_0^\infty \frac{P_0(f\theta/U_\infty)}{\tau_w^2}\,\frac{U_\infty}{\theta}\,d\left(\frac{f\theta}{U_\infty}\right) = F(M_\infty,\ R_\theta) \tag{12}$$

Examining the integrand, as before, one obtains

$$\frac{P_0(f\theta/U_\infty)}{\tau_w^2}\,\frac{U_\infty}{\theta} = G\left(\frac{f\theta}{U_\infty},\ M_\infty,\ R_\theta\right) \tag{13}$$

---

[24] The author is indebted to Professor Donald Coles, California Institute of Technology, for helpful discussions on this approach.

The problem thus reduces to one of determining the unknown functions G and $\mathcal{G}$, respectively, in Eqs. (10) and (13).

Spectrum plots, nondimensionalized according to Eqs. (10) and (13), are presented in Fig. 16. By integrating the spectra, using Eqs. (8) and (11), and extracting their square roots, the ratios of $\tilde{p}/q_\infty$ and $\tilde{p}/\tau_w$, respectively, are obtained as a function of freestream Mach number and Reynolds number, where $\tilde{p}$ is the root-mean-square value of the total fluctuating pressure. These ratios are presented in Fig. 17.

C. Space-Time Correlations

The correlation of the noise in time and in space are obtained by taking measurements at two points on the plate and using the relationship

$$R(\tau) = \frac{\overline{(e_1^2 - e_2^2)} - \overline{(e_1 - e_2)^2}}{2\,(\overline{e_1^2})^{1/2}\,(\overline{e_2^2})^{1/2}} = \frac{\overline{e_1\,e_2}}{(\overline{e_1^2})^{1/2}\,(\overline{e_2^2})^{1/2}} \qquad (14)$$

where $R(\tau)$ is defined as the correlation function, e_1 is the signal measured at the upstream point x at time $(t - \tau)$, and e_2 is the signal measured at the downstream point $(x + \Delta x)$ at time t. The bar denotes ensemble average, which, for the type of process considered here, will be equal to the time average. Typical correlation measurements are given in Fig. 18 for Mach numbers ranging from 2 to 5.

The velocity at which the noise is convected downstream is determined from the correlation data using the simple relationship

$$V_c = \frac{\Delta x}{\tau_{opt}} \tag{15}$$

where V_c = the convection velocity, Δx = the spacing between pickup points, and τ_{opt} = the time interval required to travel from upstream point to downstream point; i.e., the time to optimum correlation. The ratio of V_c/U_∞ is presented versus Mach number and Reynolds number in Fig. 19. Ratios of $(U_\infty - V_c)/a_\infty$ and V_c/a_w vs M_∞ are given in Fig. 20, where a_∞ is the sound speed in the freestream and a_w is the sound speed based on the adiabatic wall temperature.

V. RESULTS AND CONCLUSIONS

The spectral density reaches an asymptotic value as zero frequency is approached, and it shows a characteristic roll-off at the high frequencies. The nondimensional spectrum based on freestream dynamic pressure (Fig. 16a) gives good similarity at high frequencies, but exhibits a definite dependence on Reynolds number at low frequencies. The Reynolds number dependence is of the order of $R_{\delta^*}^{-1/5}$ when the spectral energy data are presented in the form of $\tilde{p}/q_\infty$ (Fig. 17a), where p is the root-mean-square value of the total fluctuating pressure and q_∞ is the freestream dynamic pressure.

The dependence on $R_{\delta^*}^{-1/5}$ suggests the use of τ_w, the shear at the wall, in the nondimensionalization, since the local skin friction in a turbulent boundary layer, $C_f = \tau_w/q_\infty$, is also related to the Reynolds number in a similar manner. The resulting spectra (Fig. 16b) show good similarity throughout the range of frequencies, without any apparent dependence on either Reynolds number or Mach number. The scatter in the data is attributable to small variations in the measurement of the momentum thickness θ. On the basis of this experimental evidence, the functional relationship in Eq. (13) may be simplified to give

$$\frac{\Phi_0(f\theta/U_\infty)}{\tau_w^2}\,\frac{U_\infty}{\theta} = G\,(f\theta/U_\infty) \tag{16}$$

The value of $\tilde{p}$, when based on τ_w (Fig. 17b), is also invariant with Reynolds number; it is invariant with Mach number except, perhaps, when $M_\infty = 5$ is approached. Thus, the mean square value of the total fluctuating pressure in Eq. (11) may be reduced to

$$\frac{\overline{p'^2}}{\tau_w^2} = \text{constant} \simeq 100 \tag{17}$$

Inasmuch as $\tau_w = C_f q_\infty$ and $q_\infty = (\gamma/2)pM_\infty^2 = 0.7\,pM_\infty^2$ for air, $\overline{p'^2}$, in terms of the freestream Mach number, may be written

$$\frac{\overline{p'^2}}{p^2} \simeq 50\,C_f^2 M_\infty^4 \tag{18}$$

The convection velocity of the pressure fluctuations is determined from the space-time correlation data (Fig. 18) and using Eq. (15). Most of the measurements were made at $\Delta x = 0.25$ and 0.50 in.; a few were made at $\Delta x = 1$ in. A constant ratio of convection velocity to freestream velocity equal to

$$\frac{V_c}{U_\infty} \simeq 0.75 \tag{19}$$

is obtained, independent of both Mach number and Reynolds number (Fig. 19). The ratio of V_c/U_∞ for the measurements at $\Delta x = 0.25$ in. are about 5% lower than those at the other spacings. This difference corresponds to an error of about 0.005 in. in the measurement of the center-to-center distance between pickup points, which in this case, are circular areas of 0.03 in. diameter.

The existence of a characteristic or bulk velocity of convection implies that V_c rather than U_∞ may be the more appropriate parameter to use in the nondimensional energy spectrum. This corresponds to a change of Eq. (16) to

$$\frac{\Phi_0(f\theta/V_c)}{\tau_w^2} \frac{V_c}{\theta} = G\left(\frac{f\theta}{V_c}\right) \tag{20}$$

In constrast to Eq. (16), Eq. (20) will result in a decrease of 25% in the ordinate and an increase of 25% in the abscissa in the spectral data as presented in Fig. 16b, in accordance with the relationship between V_c and U_∞ in Eq. (19).

A point of interest is the magnitude of the velocity of convection in relation to the speed of sound. The comparison is made relative to a_∞, the sound speed in the freestream (Fig. 20a), and a_w, the sound speed at the adiabatic wall (Fig. 20b). In both instances, sonic velocity is reached above $M_\infty = 1$. In the former case $(U_\infty - V_c)/a_\infty = 1$ at $M_\infty \simeq 3.5$; in the latter case, $V_c/a_w = 1$ when $M_\infty \simeq 1.5$.

The rate of decay of the convection noise in the streamwise direction may be determined from a measure of the degree of correlation (for optimum correlation) as a function of the time of delay for several pickup spacings. An estimate of this may be obtained from the fact that (1) the fluctuation noise is only 6% correlated for a spacing of $\Delta x = 1$ in., and (2) the degree of correlation diminishes by a factor of 4 or 5 when the pickup spacing is increased by a factor of 4 (from 0.25 to 1 in.). The sudden drop from $R(0) = 1$ for zero spacing to $R(\tau_{opt}) = 0.25$ at $\Delta x = 0.25$ in. is the result of the phase shift and limited response of the LC time delay unit. A more precise rate of decay would require the use of a time delay with better response and phase characteristics.

APPENDIX A

Spectral Measurements in Subsonic Flow

The spectral measurements presented in the manuscript may be compared with those obtained at subsonic flow conditions. Willmarth[12] concludes that the fluctuating pressure based on dynamic pressure is a constant equal to $\frac{\tilde{p}}{q_\infty} = 0.006$ for Mach numbers between $0.3 < M_\infty < 0.7$ and Reynolds numbers between $10^4 < R_{\delta^*} < 5 \times 10^4$. The wide-band measurements of $\tilde{p}$ were made using a vacuum-tube voltmeter which has been calibrated against a true root-mean-square meter. The effect of finite transducer size was accounted for by extrapolation of the measured data of $\frac{\tilde{p}}{q_\infty}$ to a crystal pickup of zero size.

The use of a voltmeter for root-mean-square averaging is not as rigorous as actual numerical integration of the energy spectrum. Neither is the method of extrapolating to zero pickup size strictly correct, since $\frac{\tilde{p}}{q_\infty}$ is, in general, actually dependent on variations in both Mach number and Reynolds number, rather than on the parameter d/δ^*. A close examination of Willmarth's spectral data shows a possible dependence on Reynolds number at the lower frequencies, although the dependence on Mach number is hidden by the limited test range and by the scatter in the experimental data.

In order to provide a common basis for comparison, several representative sets of spectral data from Willmarth's measurements were recomputed employing the same approach as that of the present

investigation, including corrections for frequency and amplitude attenuation due to transducer size. Values of shear at the wall were obtained using the appropriate C_f for incompressible flow. The resulting nondimensional spectra are shown in Fig. A-1. Integration of these spectra yield the curves of $\frac{\tilde{p}}{q_\infty}$ and $\frac{\tilde{p}}{\tau_w}$ in Fig. A-2.

It may be seen that the corrected spectra in subsonic flow have distinctly lower values than those in supersonic flow. The integrated values of $\frac{\tilde{p}}{q_\infty}$ show a dependence on Reynolds number and are lower than the extrapolated values by a factor of 2 to 3. The corresponding values of $\frac{\tilde{p}}{\tau_w}$ are about 10 times lower than those in supersonic flow, indicating a noise environment which may be an order of magnitude more severe in supersonic flow than in subsonic flow.

APPENDIX B

List of Electronic Equipment

Make	Model	Type	Description	Range
AE		606	Variable delay line	0-120 μsec
Bo		260A	Q meter	50 kc - 50 Mc
Br	156X15[V]		Potentiometer pyrometer	0-5 mv
GR		1390A	Random noise generator	0-5 volts, 0-5 Mc
HP	300A		Harmonic wave analyzer	0-16 kc
HP	400D		Vacuum tube voltmeter	60 db
HP	450A/AR		Amplifier	20-40 db, 10 cps - 1 Mc
HP	460A		Wide-band amplifier	30 db, 100 kc-100 Mc
HP	524B		Electronic counter	1 msec to 1 sec
HP	650A		Test oscillator	0-10 Mc
KH	310AB		Variable band-pass filter	20 cps-200 kc
Mi			Microlab attenuator	- 60 db
Mo	2A		Autograf X-Y recorder	
Pa	Lp - 1a		Panoramic sonic analyzer	0-20 kc
Pa	SE-7a		Panoramic ultrasonic analyzer	0-200 kc
Ra			Micro ammeter	0-50 μamps

Make	Model	Type	Description	Range
SE	A-50B		Hot wire anemometer, amplifier	1 cps-320 kc
SE	A-40-BM		Wide band amplifier	1 cps-800 kc
Sl	121		Wave analyzer	15 kc-500 kc
So	10000S		AC voltage regulator	120 volts
St			Pressure gauge	10 psia
TC		21	Vacuum thermocouple, insulated heater	1.5 ma
Tk		535 551	Oscilloscope Dual beam oscilloscope	

APPENDIX C

Abbreviations of Manufacturers' Names

AE	Advanced Electronics Laboratories, Inc., Passaic, New Jersey
Bo	Boonton Radio Corporation, Boonton, New Jersey
Br	Minneapolis-Honeywell, Brown Instrument Division, Minneapolis, Minnesota
GR	General Radio Company, Cambridge, Massachusetts
HP	Hewlett-Packard, Palo Alto, California
KH	Krohn-Hite Instrument Company, Cambridge, Massachusetts
Mo	F. L. Moseley Company, Pasadena, California
Pa	Panoramic Radio Products, Inc., Mt. Vernon, New York
Ra	Rawson Electrical Instruments Company, Cambridge, Massachusetts
SE	Shapiro-Edwards, South Pasadena, California
Si	Sierra Electronic Corporation, San Carlos, California
So	Sorenson and Company, Inc., Stamford, Connecticut
St	Statham Instruments, Inc., Los Angeles, California
TC	American Thermo-Electric Company, New York, New York
TK	Tektronix, Inc., Portland, Oregon

FIGURES

1. JPL 12-in. supersonic wind tunnel with model installed in test section 33

3. Flat plate installed in 20-in. tunnel test section with boundary-layer probe positioned over transducer station. . . . 30

3a. Front view of plate insert showing typical flush mounting of the pressure transducers 31

3b. Rear view of plate insert showing terminal connections 32

4. Barium titanate pressure transducer 33

5. Shock tube and equipment used for calibration of pressure transducer 34

6a. Typical oscilloscope photographs of transducer response to shock waves $\Delta V \simeq 4$ mv; $\Delta p \simeq 1$ psi; sweep from left to right at 10^{-4} sec/div 36

6b. Sensitivity calibrations of two typical pressure transducers Crystal A = 0.015 in. D, Crystal B = 0.030 in. D 35

7. Electronic equipment for measuring energy spectrum 36

8. Electronic equipment for measuring space-time correlation . . 37

9. Calibration of the time delay with the autocorrelation of a random noise signal 38

10. Typical data plot of pitot traverse across the turbulent boundary layer 39

FIGURES (Cont'd)

11a. Typical velocity profiles for determination of boundary-layer displacement thickness δ^* over transducer measuring station 40

11b. Typical velocity profiles for determination of boundary-layer momentum thickness θ over transducer measuring station 41

12. Typical data plot of energy spectrum showing amplitude distribution with frequency. 42

13. Corrections applied to typical power spectrum 43

14. Frequency attenuation of energy spectrum due to size and shape of pressure transducer 44

15. Amplitude attenuation of energy spectrum assuming isotropic turbulence of flow in plane of flat plate 45

16a. Non-dimensional spectrum based on freestream dynamic pressure; M_∞ = 2.01 to 5.00 46

16b. Non-dimensional spectrum based on the shear at the wall; M_∞ = 2.01 to 5.00 47

17a. Root-mean-square levels of noise based on freestream dynamic pressure; M_∞ = 2.01 to 5.00 48

17b. Root-mean-square levels of noise based on shear at the wall; M_∞ = 2.01 to 5.00 49

FIGURES (Cont'd)

18. Space-time correlations of noise on the flat plate at M_∞ = 2.01 to 5.00 50

19a. Ratio of convection velocity to freestream velocity as a function of Mach number 51

19b. Ratio of convection velocity to freestream velocity as a function of Reynolds number. 52

20a. Ratio of convection velocity to sound speed in the freestream as a function of Mach number 53

20b. Ratio of convection velocity to sound speed at the wall as a function of Mach number 54

A-1. Non-dimensional spectra at subsonic speeds 55

A-2. Root-mean-square levels of noise at subsonic speeds 56

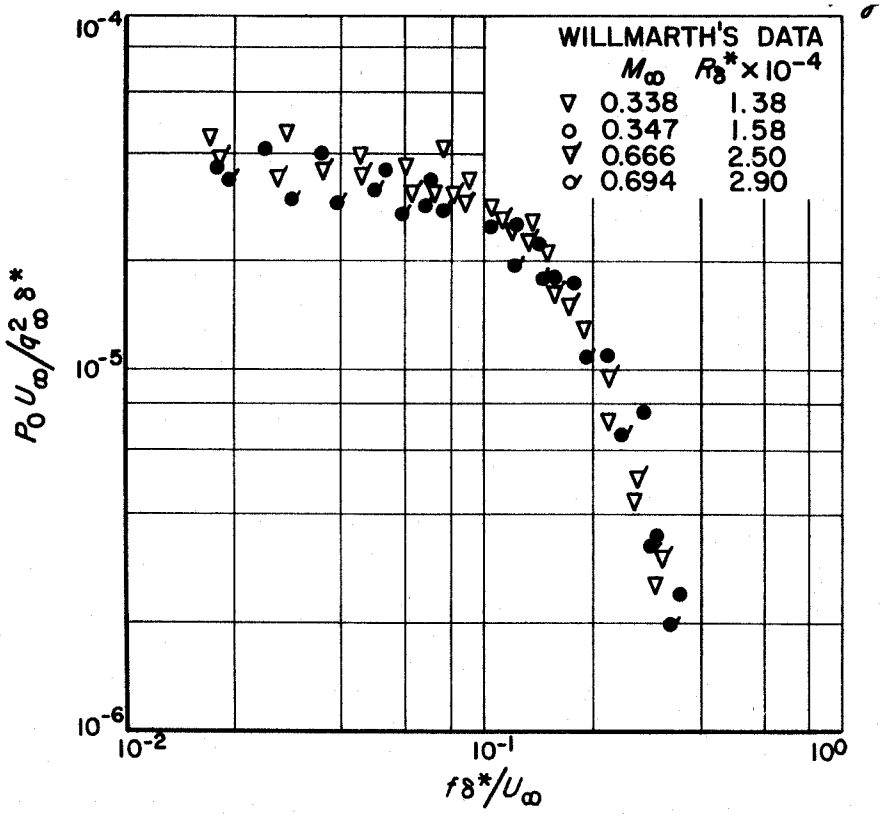
WILLMARTH'S DATA
M_∞ $R_{\delta^*}\times10^{-4}$
0.338 1.38
0.347 1.58
0.666 2.50
0.694 2.90
10^{-4}
10^{-5}
10^{-6}
10^{-2}
10^{-1}
10^{0}
$P_0 U_\infty / q^2_\infty \delta^*$
$f\delta^*/U_\infty$

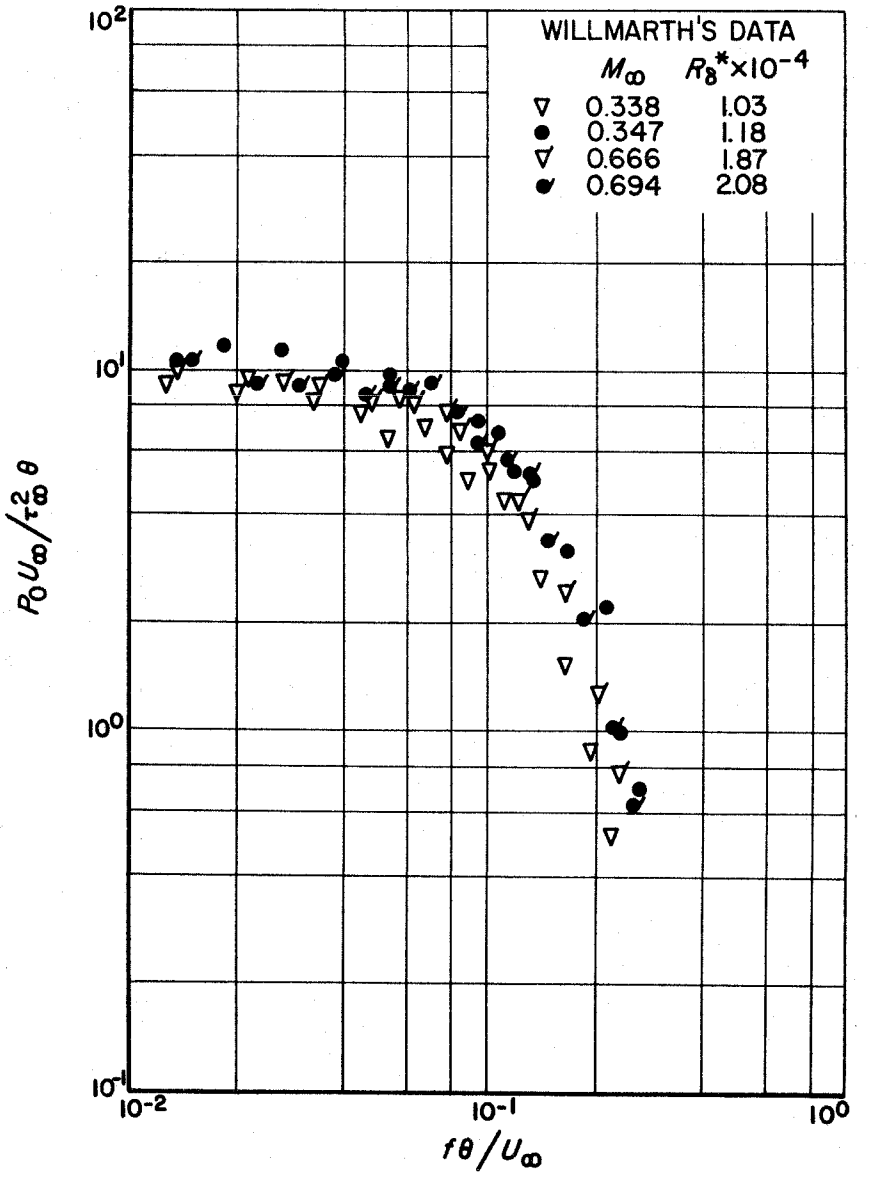
WILLMARTH'S DATA
M_∞ $R_{\delta^*}\times10^{-4}$
0.338 1.03
0.347 1.18
0.666 1.87
0.694 2.08
10^{2}
10^{1}
10^{0}
10^{-1}
10^{-2}
10^{-1}
10^{0}
$P_0 U_\infty / \tau^2_\infty \theta$
$f\theta/U_\infty$

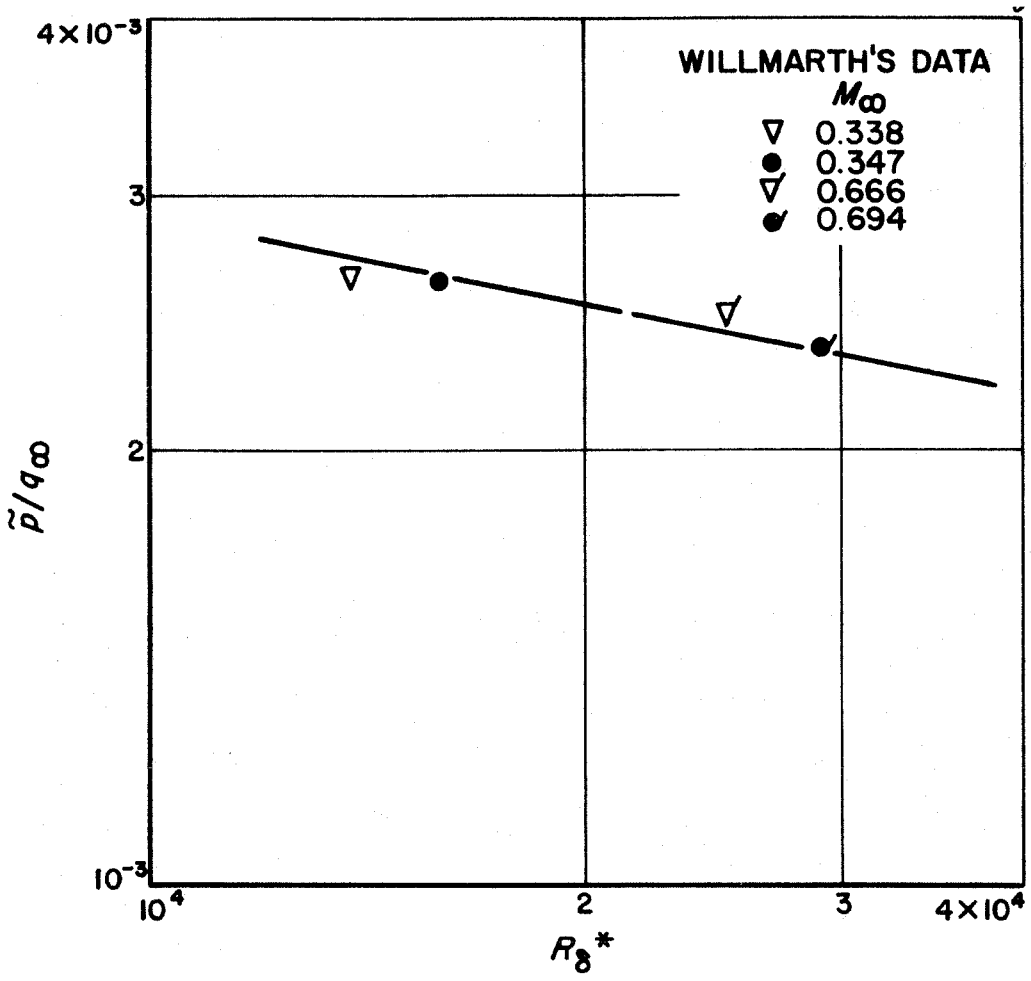
WILLMARTH'S DATA
M_∞
0.338
0.347
0.666
0.694
4×10^{-3}
3
2
10^{-3}
$\tilde{p}/q_\infty$
10^4
2
3
4×10^4
$R_\delta{}^*$

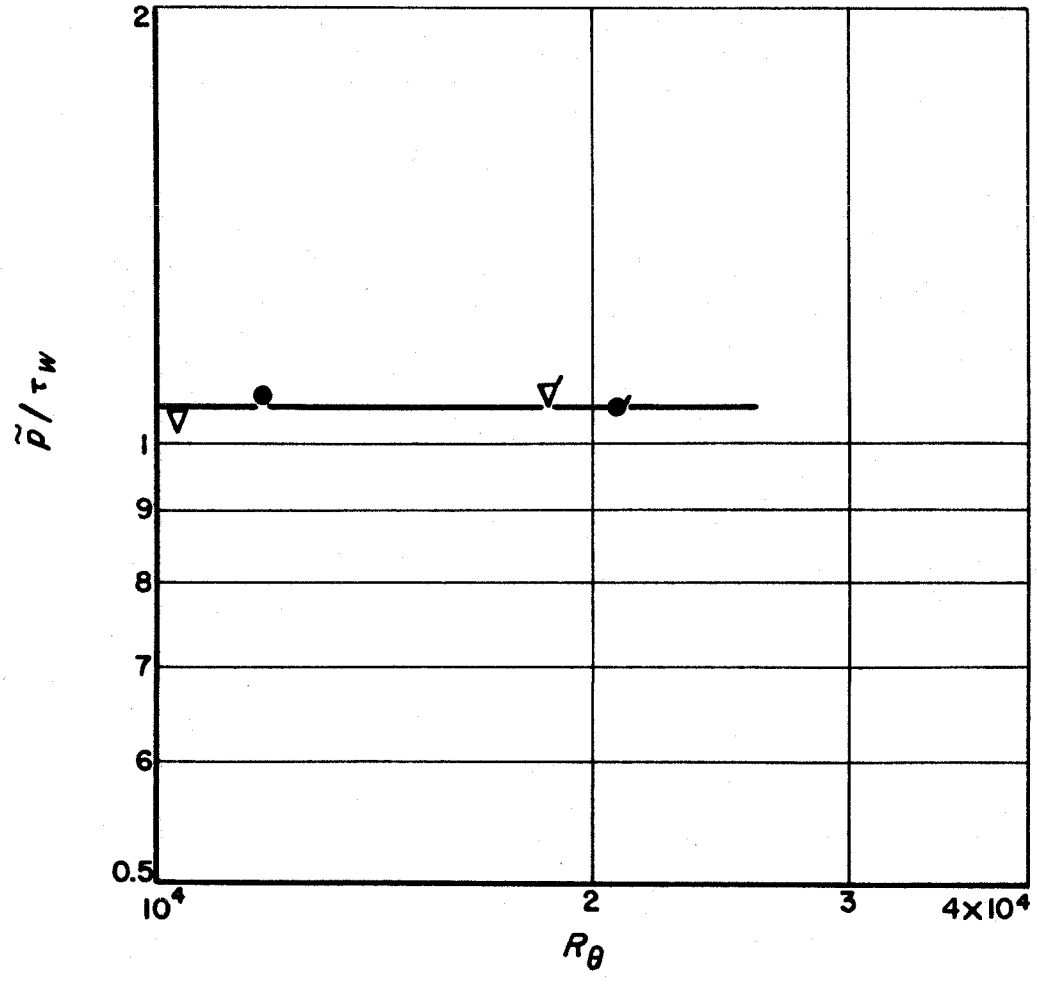
2
1
9
8
7
6
0.5
$\tilde{p}/\tau_w$
10^4
2
3
4×10^4
R_θ

Fig. 1

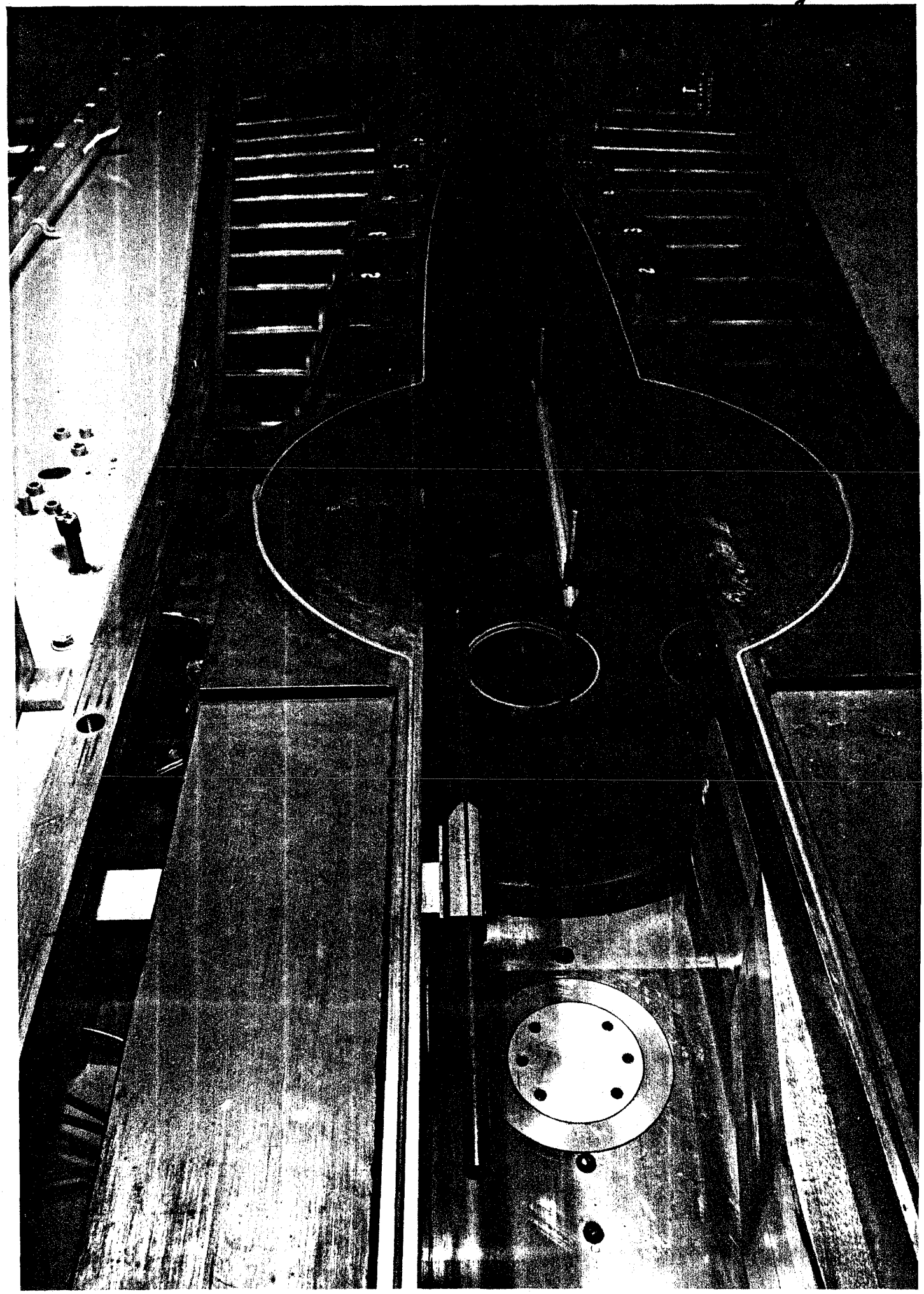

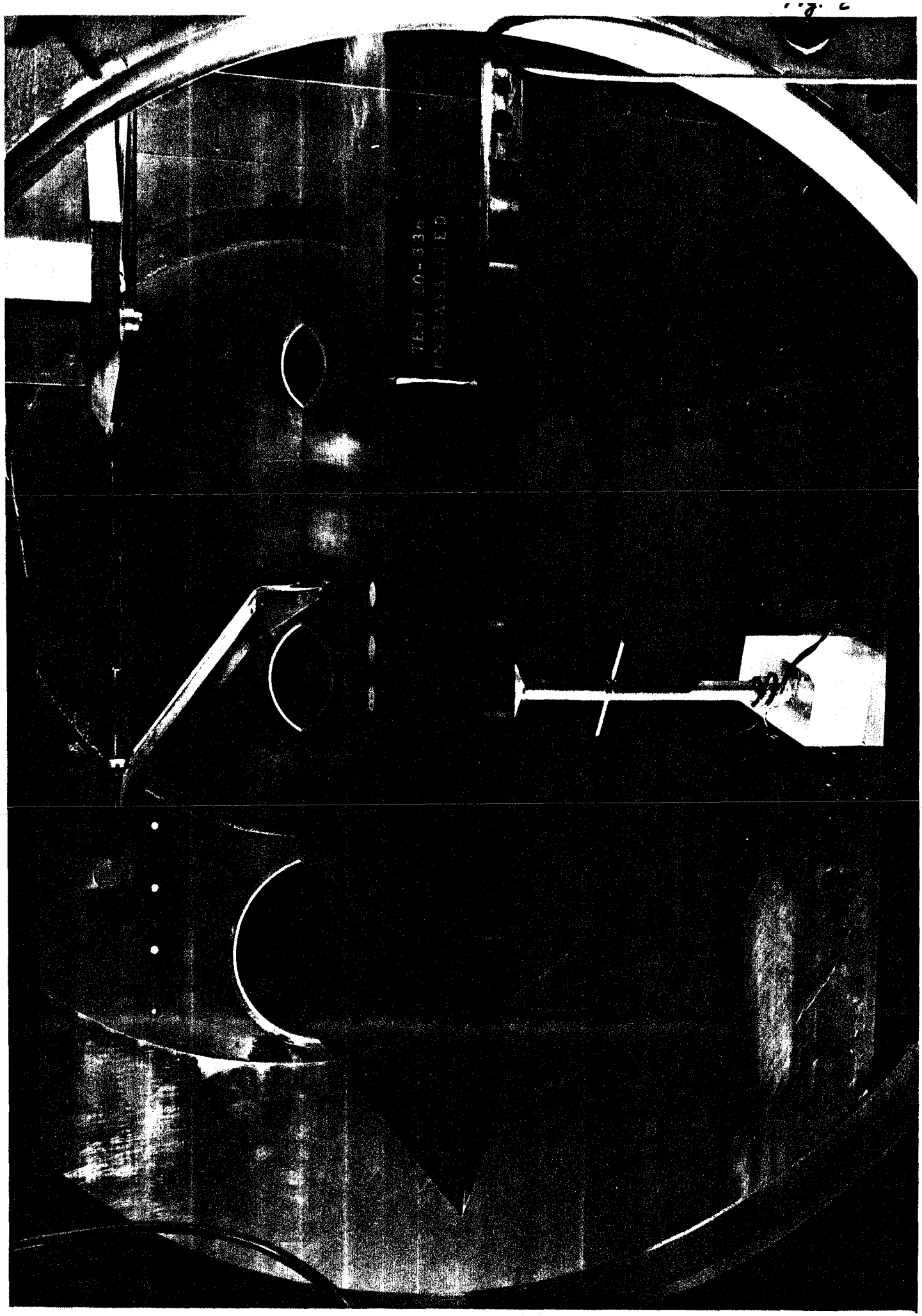
TEST 20-336
UNCLASSIFIED

Fig 3a

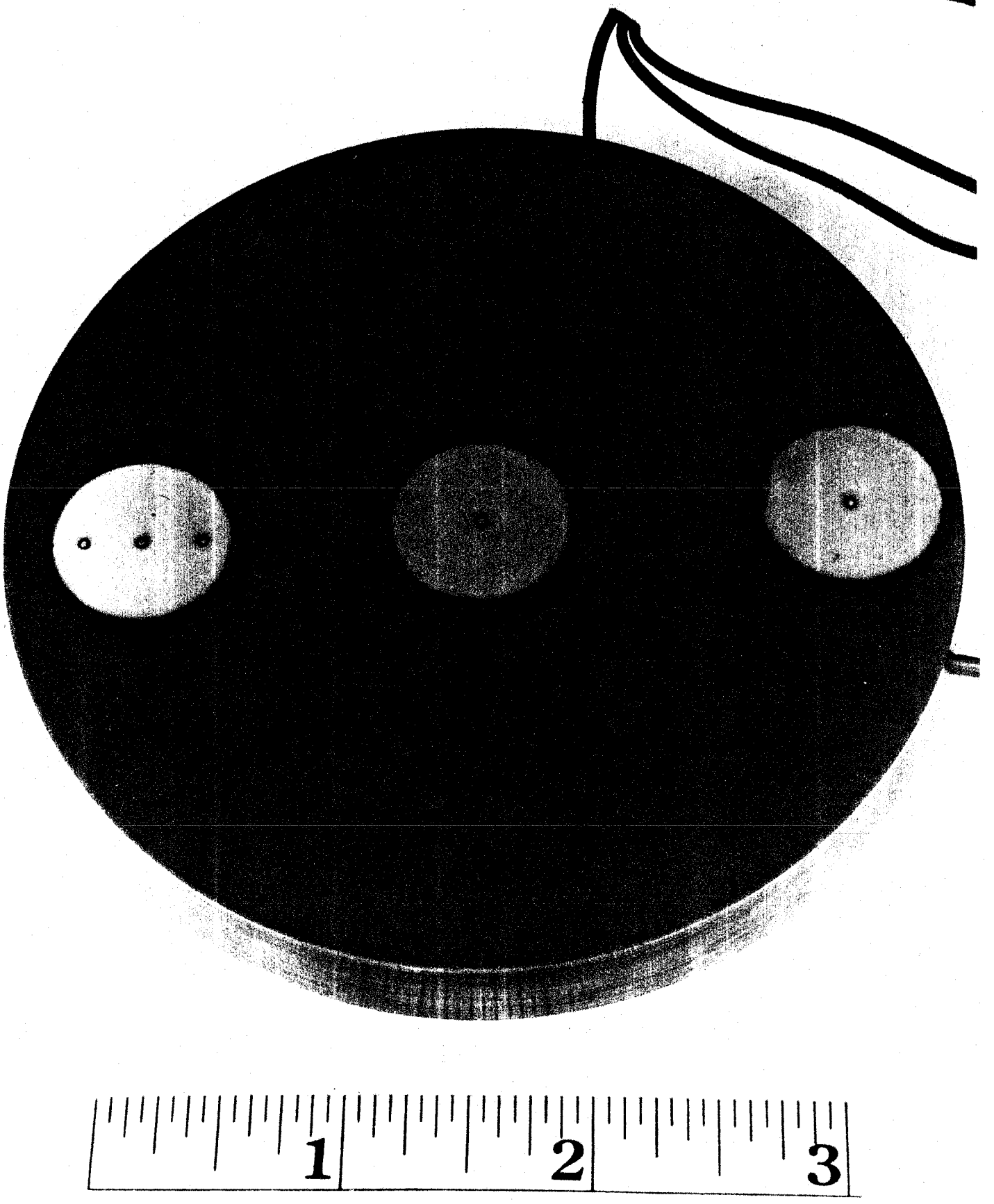

Fig 2a

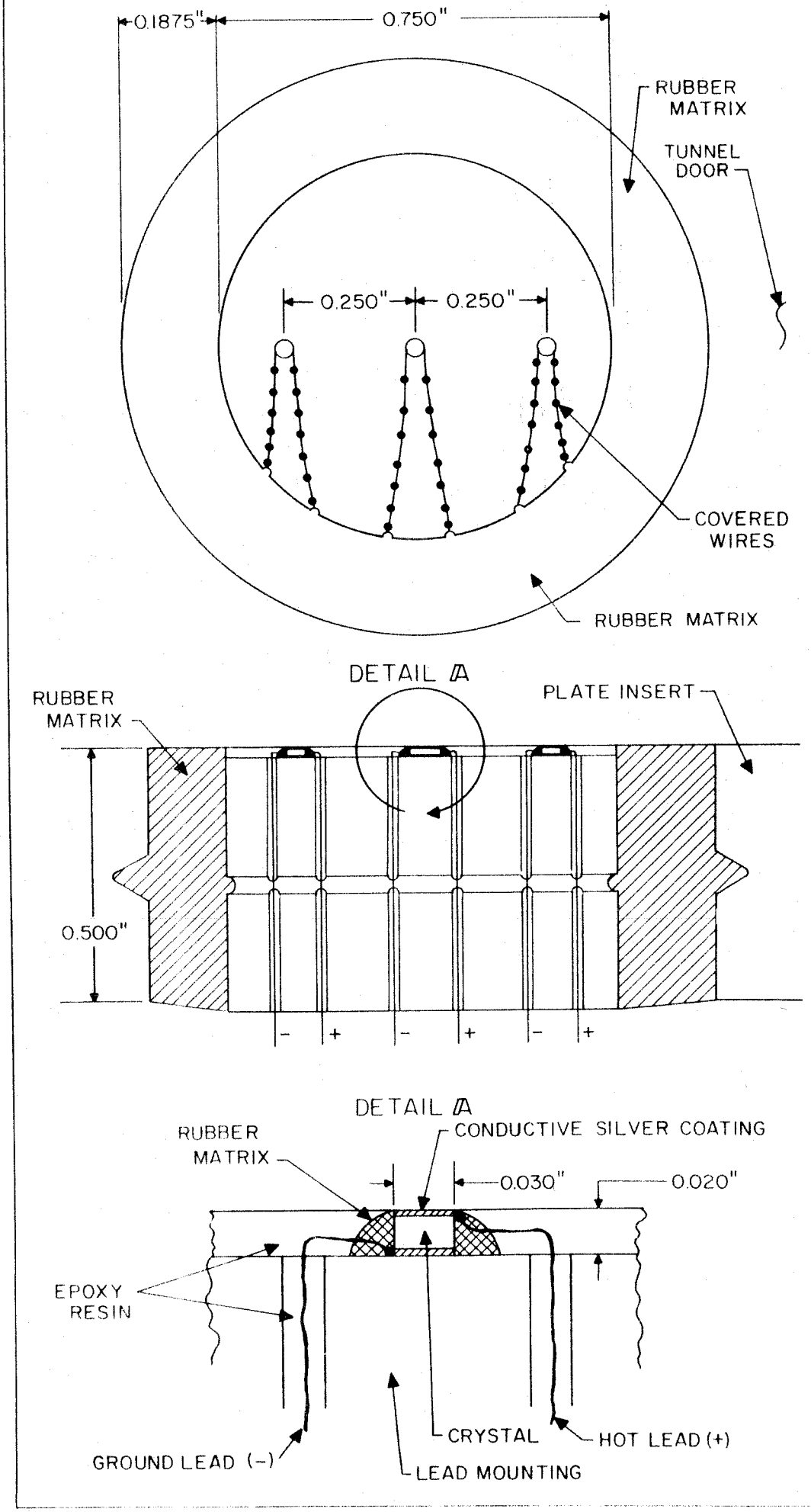
0.1875"
0.750"
RUBBER MATRIX
TUNNEL DOOR
0.250"
0.250"
COVERED WIRES
RUBBER MATRIX
DETAIL A
RUBBER MATRIX
PLATE INSERT
0.500"
- + - + - +
DETAIL A
RUBBER MATRIX
CONDUCTIVE SILVER COATING
0.030"
0.020"
EPOXY RESIN
GROUND LEAD (-)
CRYSTAL
HOT LEAD (+)
LEAD MOUNTING

Fig 5

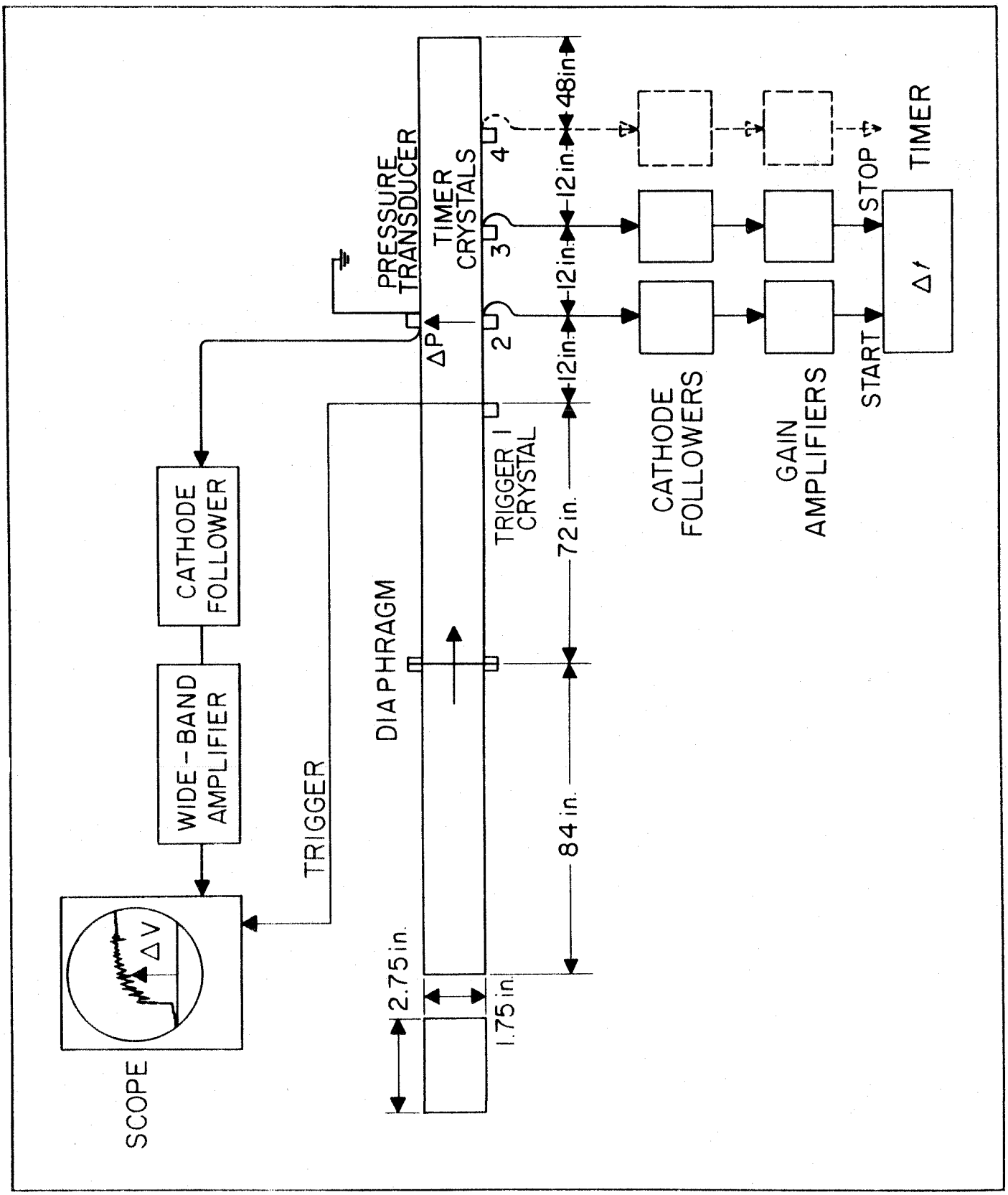
SCOPE
ΔV
WIDE-BAND AMPLIFIER
CATHODE FOLLOWER
TRIGGER
DIAPHRAGM
2.75 in.
1.75 in.
84 in.
72 in.
TRIGGER I CRYSTAL
ΔP
PRESSURE TRANSDUCER
TIMER CRYSTALS
2
3
4
12 in.
12 in.
12 in.
48 in.
CATHODE FOLLOWERS
GAIN AMPLIFIERS
START
STOP
Δt
TIMER

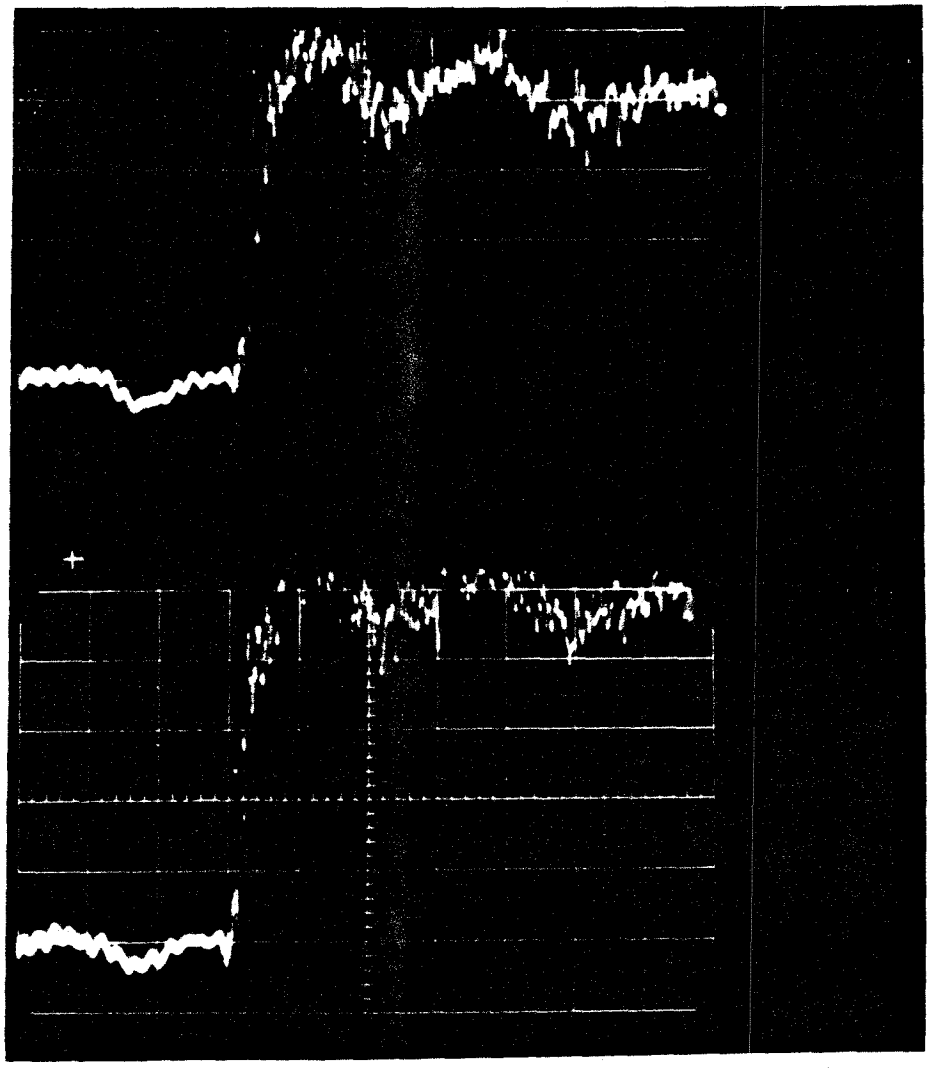

(a)

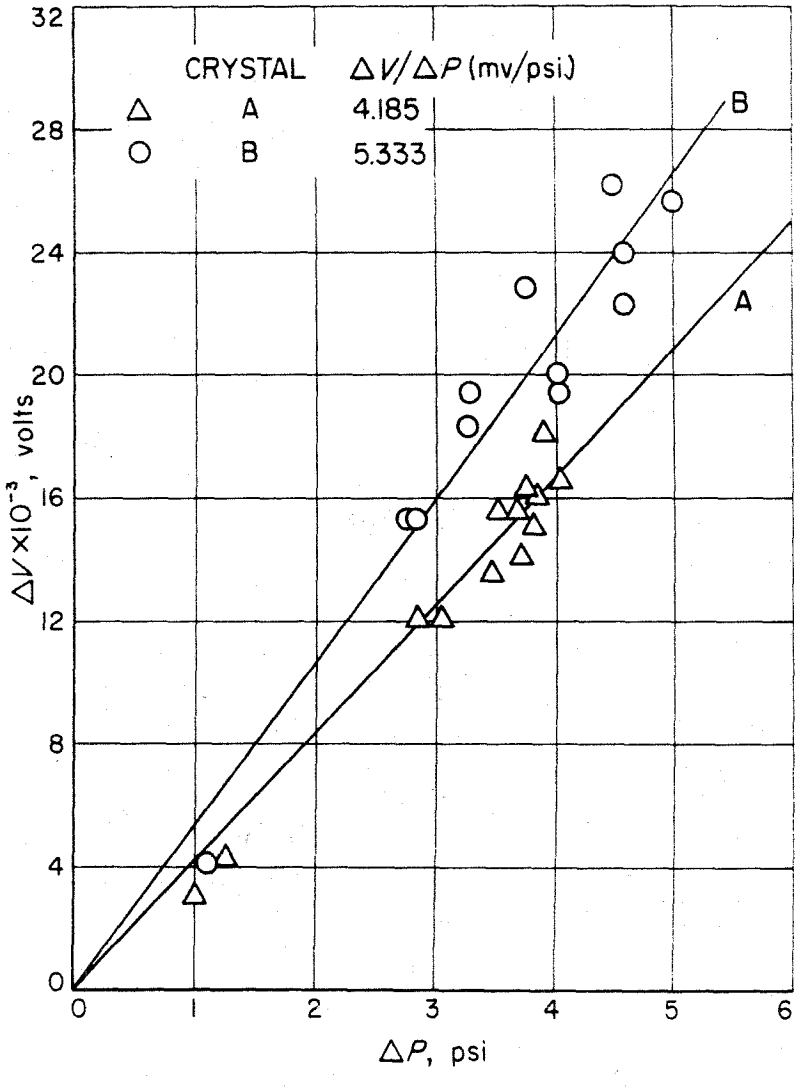
CRYSTAL
ΔV/ΔP (mv/psi)
A
4.185
B
5.333
B
A
ΔV×10⁻³, volts
ΔP, psi
0
4
8
12
16
20
24
28
32
0
1
2
3
4
5
6

(b)

Fig 9

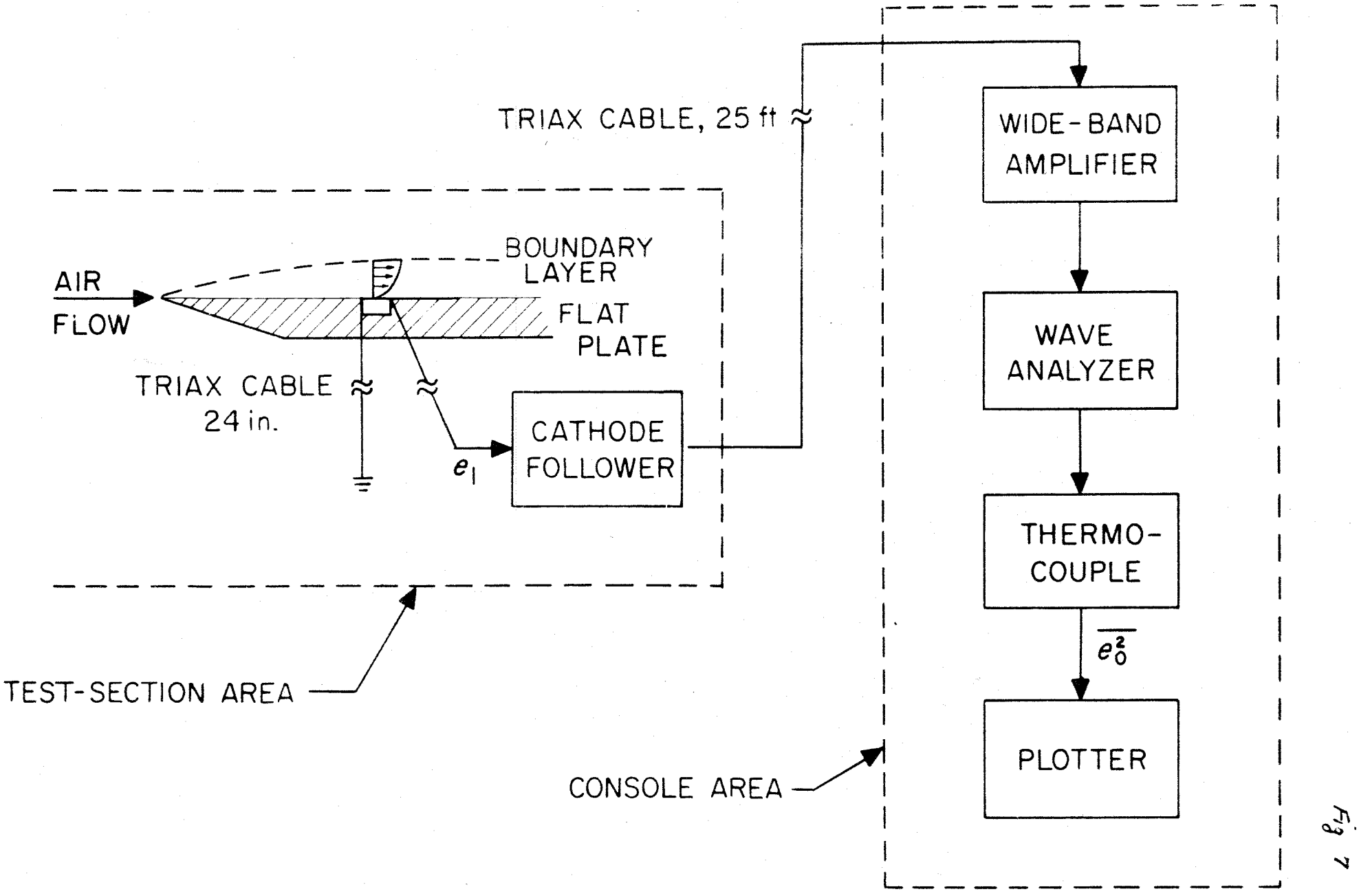
TRIAX CABLE, 25 ft
WIDE-BAND AMPLIFIER
WAVE ANALYZER
THERMO-COUPLE
$\overline{e_0^2}$
PLOTTER
BOUNDARY LAYER
AIR FLOW
FLAT PLATE
TRIAX CABLE 24 in.
e_1
CATHODE FOLLOWER
TEST-SECTION AREA
CONSOLE AREA

Fig. 7

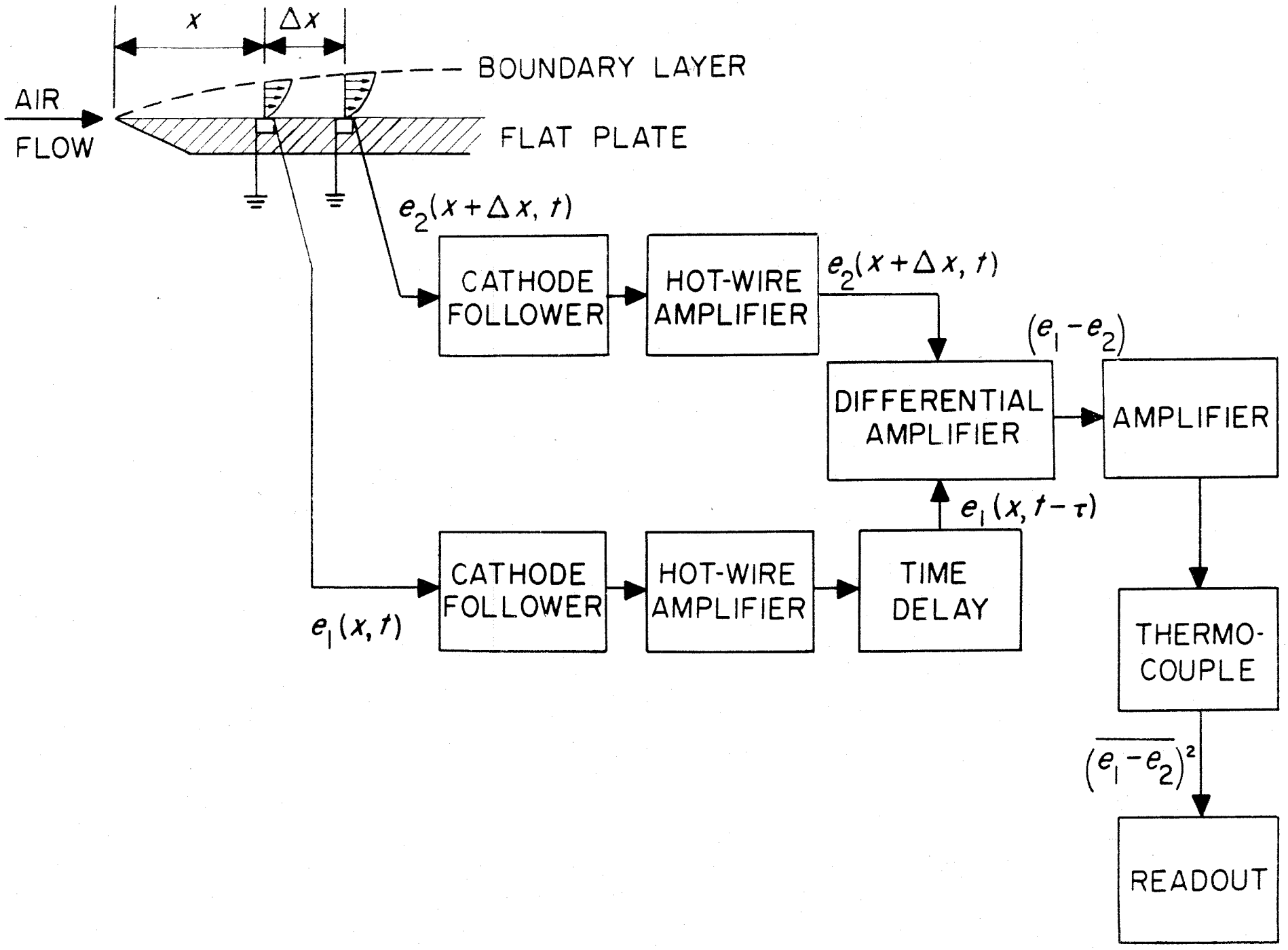
x
Δx
BOUNDARY LAYER
AIR
FLOW
FLAT PLATE
$e_2(x+\Delta x, t)$
CATHODE FOLLOWER
HOT-WIRE AMPLIFIER
$e_2(x+\Delta x, t)$
(e_1-e_2)
DIFFERENTIAL AMPLIFIER
AMPLIFIER
$e_1(x, t-\tau)$
CATHODE FOLLOWER
HOT-WIRE AMPLIFIER
TIME DELAY
$e_1(x, t)$
THERMO-COUPLE
$\overline{(e_1-e_2)^2}$
READOUT

Fig 8

Fig 9

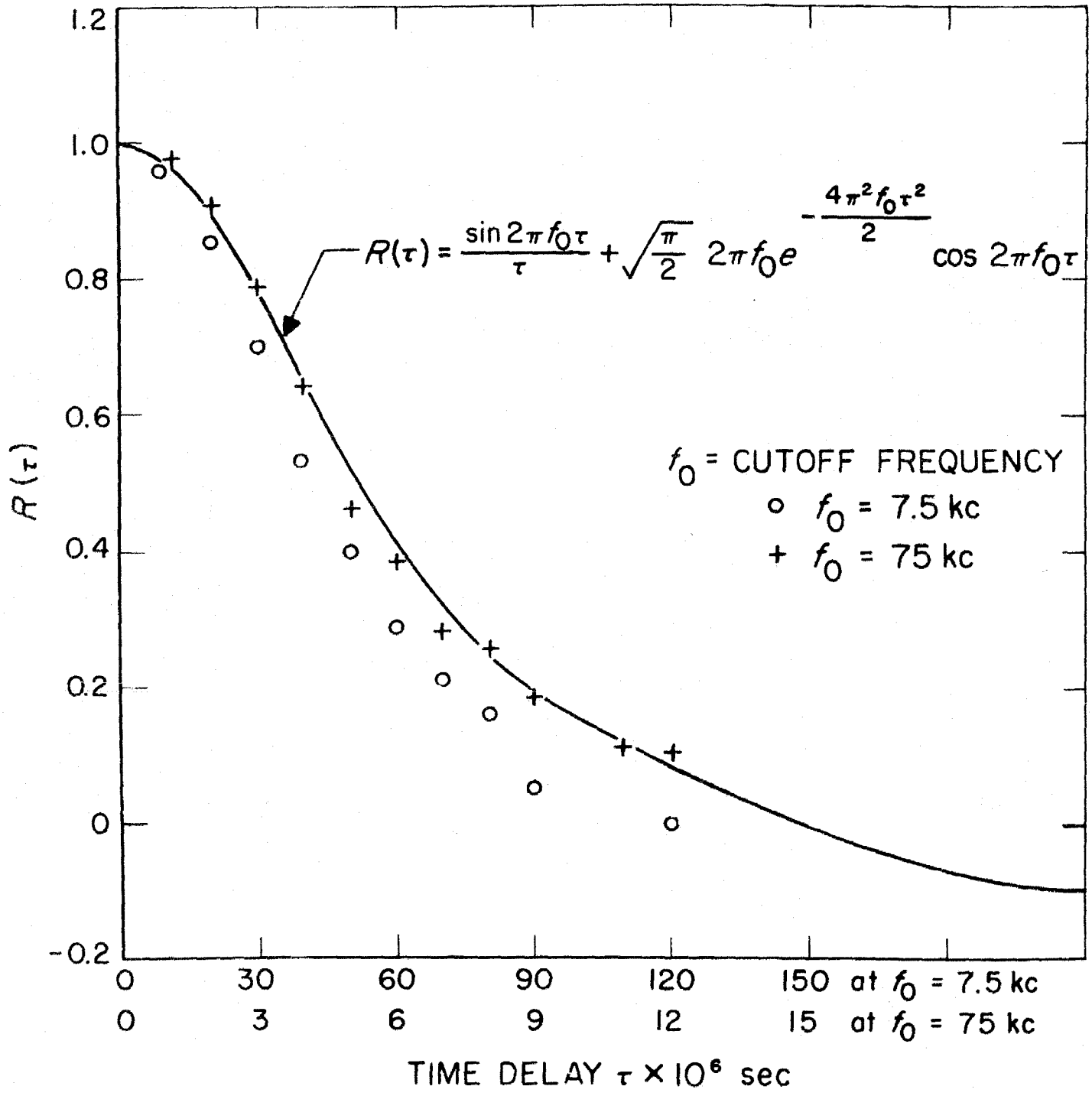
1.2
1.0
0.8
0.6
0.4
0.2
0
-0.2
R(τ)
$R(\tau) = \frac{\sin 2\pi f_0 \tau}{\tau} + \sqrt{\frac{\pi}{2}}\, 2\pi f_0 e^{-\frac{4\pi^2 f_0^2 \tau^2}{2}} \cos 2\pi f_0 \tau$
f_0 = CUTOFF FREQUENCY
o f_0 = 7.5 kc
+ f_0 = 75 kc
0 30 60 90 120 150 at f_0 = 7.5 kc
0 3 6 9 12 15 at f_0 = 75 kc
TIME DELAY τ × 10⁶ sec

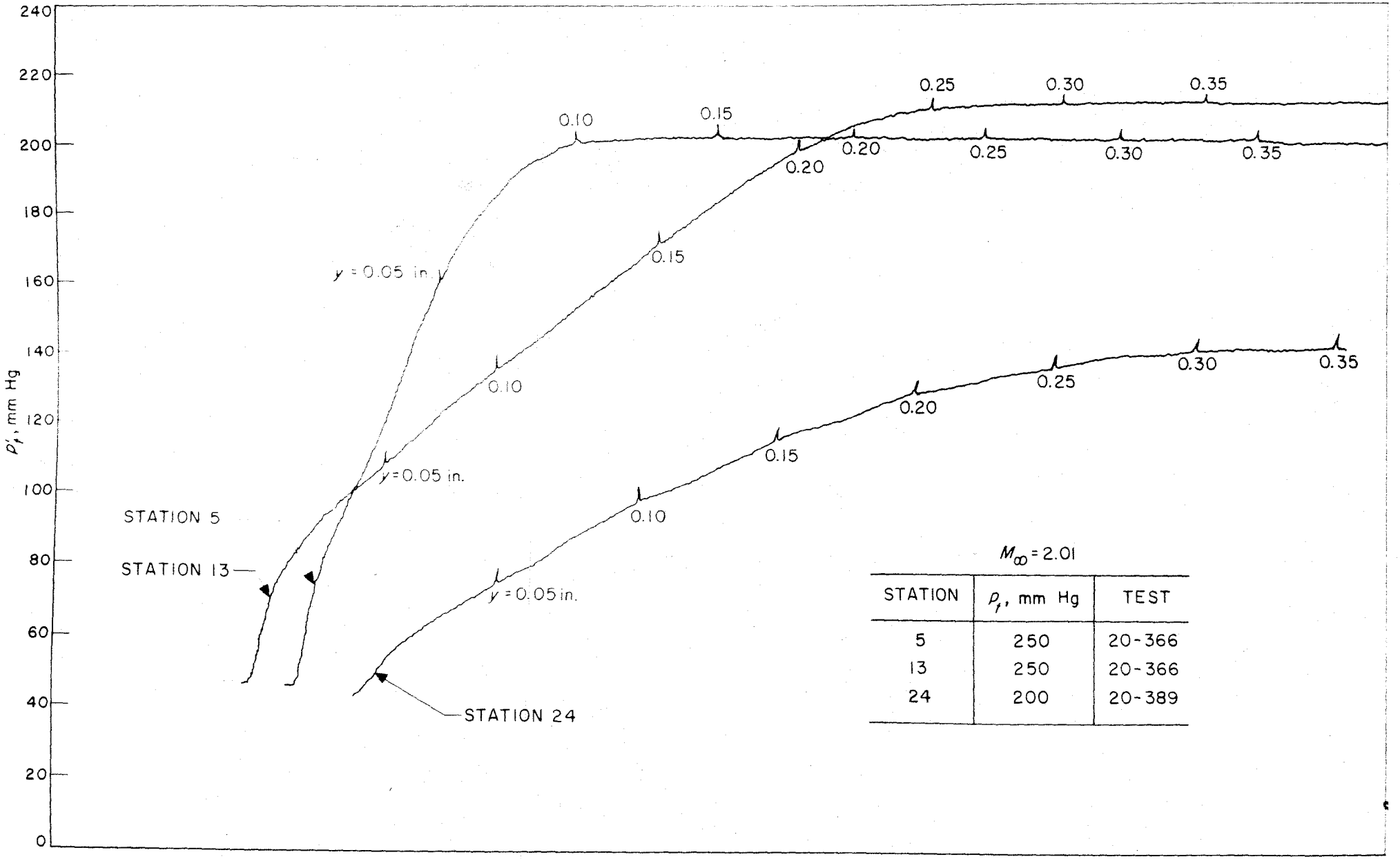
240
220
200
180
160
140
120
100
80
60
40
20
0
p_t', mm Hg
0.10
0.15
0.20
0.25
0.30
0.35
y = 0.05 in.
STATION 5
STATION 13
STATION 24
$M_\infty = 2.01$
STATION | p_t, mm Hg | TEST
5 | 250 | 20-366
13 | 250 | 20-366
24 | 200 | 20-389

Fig 11a

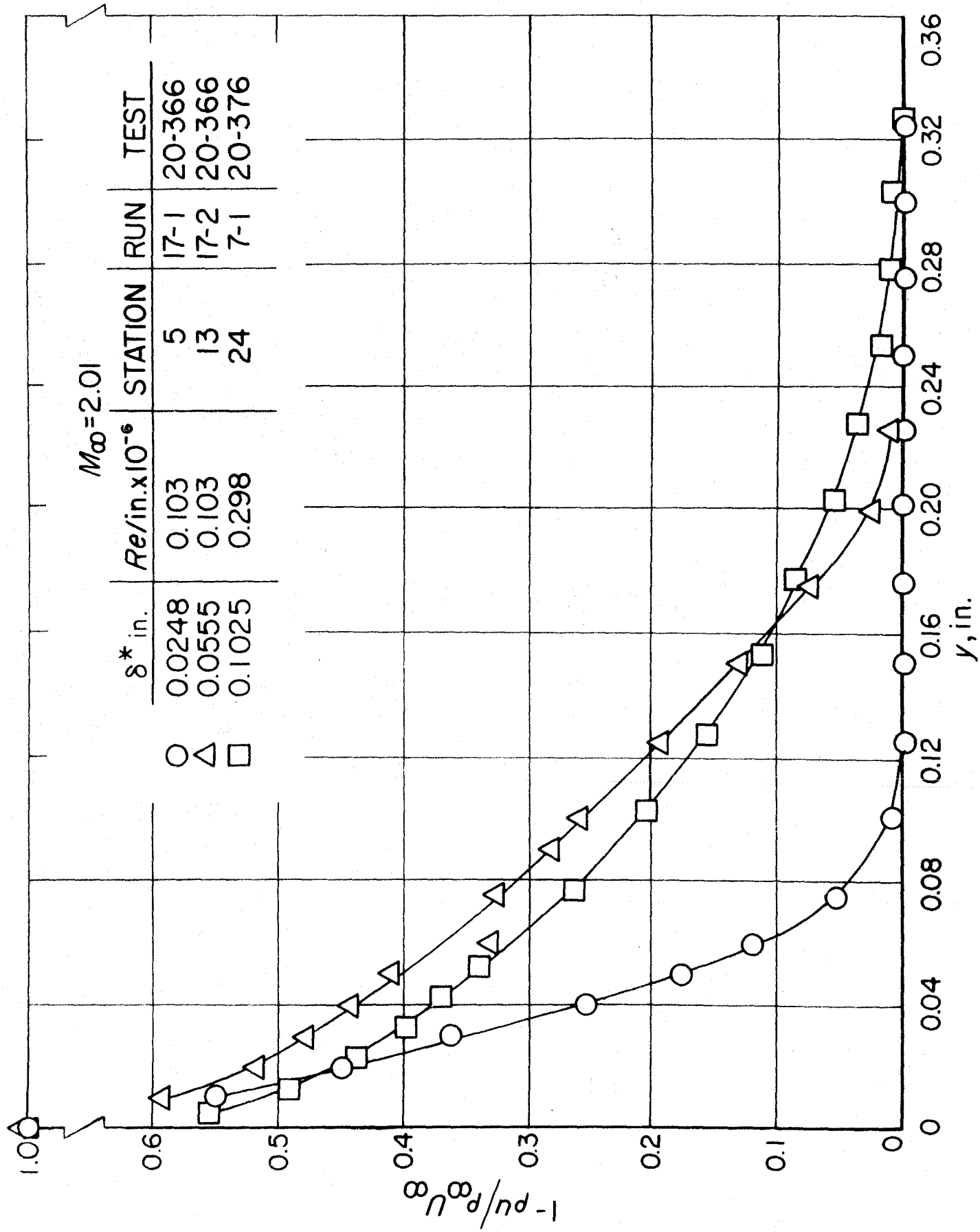
M_∞=2.01
δ* in.
Re/in.x10⁻⁶
STATION
RUN
TEST
○ 0.0248 0.103 5 17-1 20-366
△ 0.0555 0.103 13 17-2 20-366
□ 0.1025 0.298 24 7-1 20-376
1.0
0.6
0.5
0.4
0.3
0.2
0.1
0
1-ρu/ρ∞U∞
0
0.04
0.08
0.12
0.16
0.20
0.24
0.28
0.32
0.36
y, in.

Fig 11b

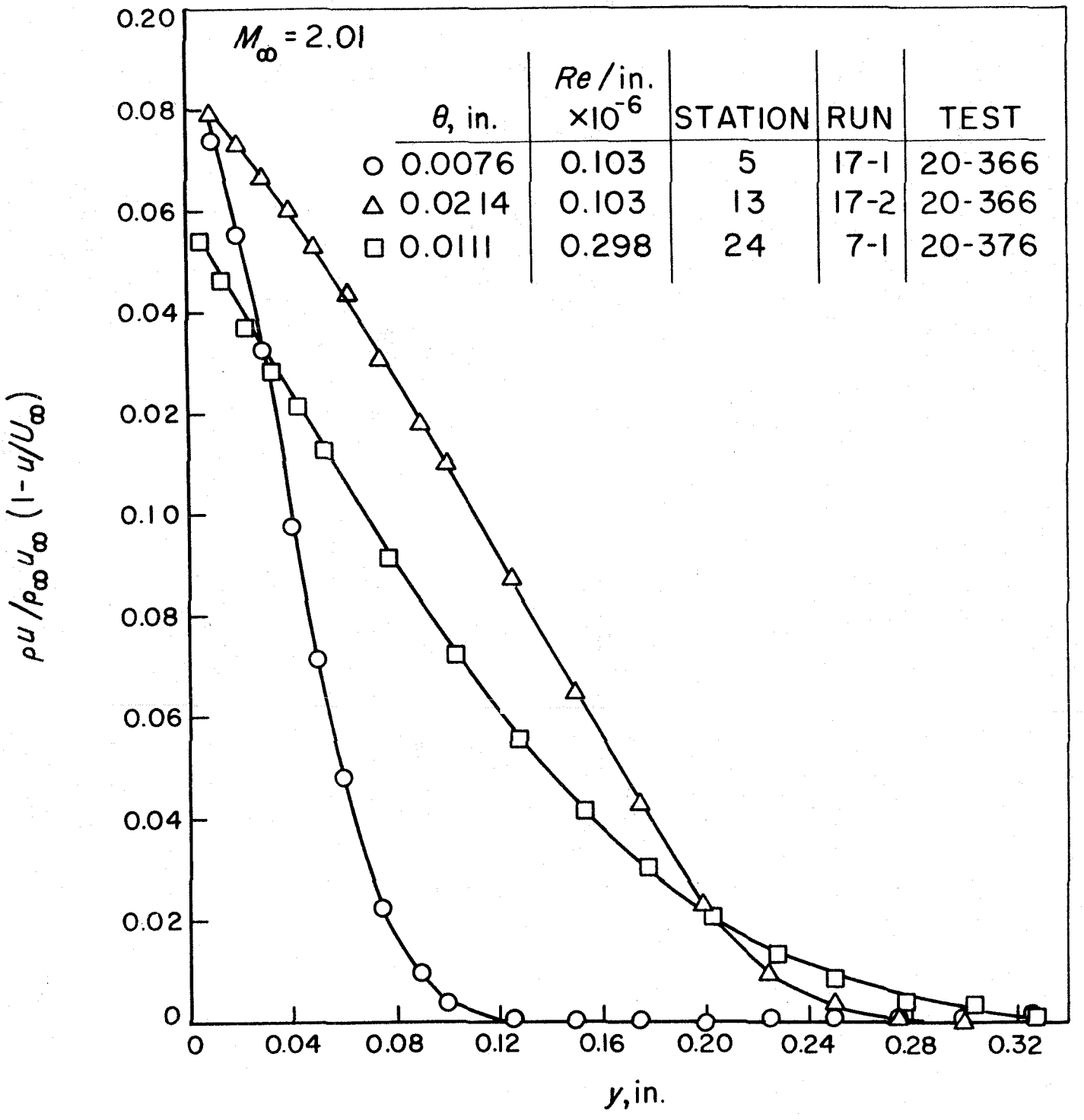
$M_\infty = 2.01$
θ, in.
Re/in. ×10⁻⁶
STATION
RUN
TEST
○ 0.0076 0.103 5 17-1 20-366
△ 0.0214 0.103 13 17-2 20-366
□ 0.0111 0.298 24 7-1 20-376
0.20
0.08
0.06
0.04
0.02
0.10
0.08
0.06
0.04
0.02
0
0 0.04 0.08 0.12 0.16 0.20 0.24 0.28 0.32
y, in.
$\rho u / \rho_\infty u_\infty (1 - u/U_\infty)$

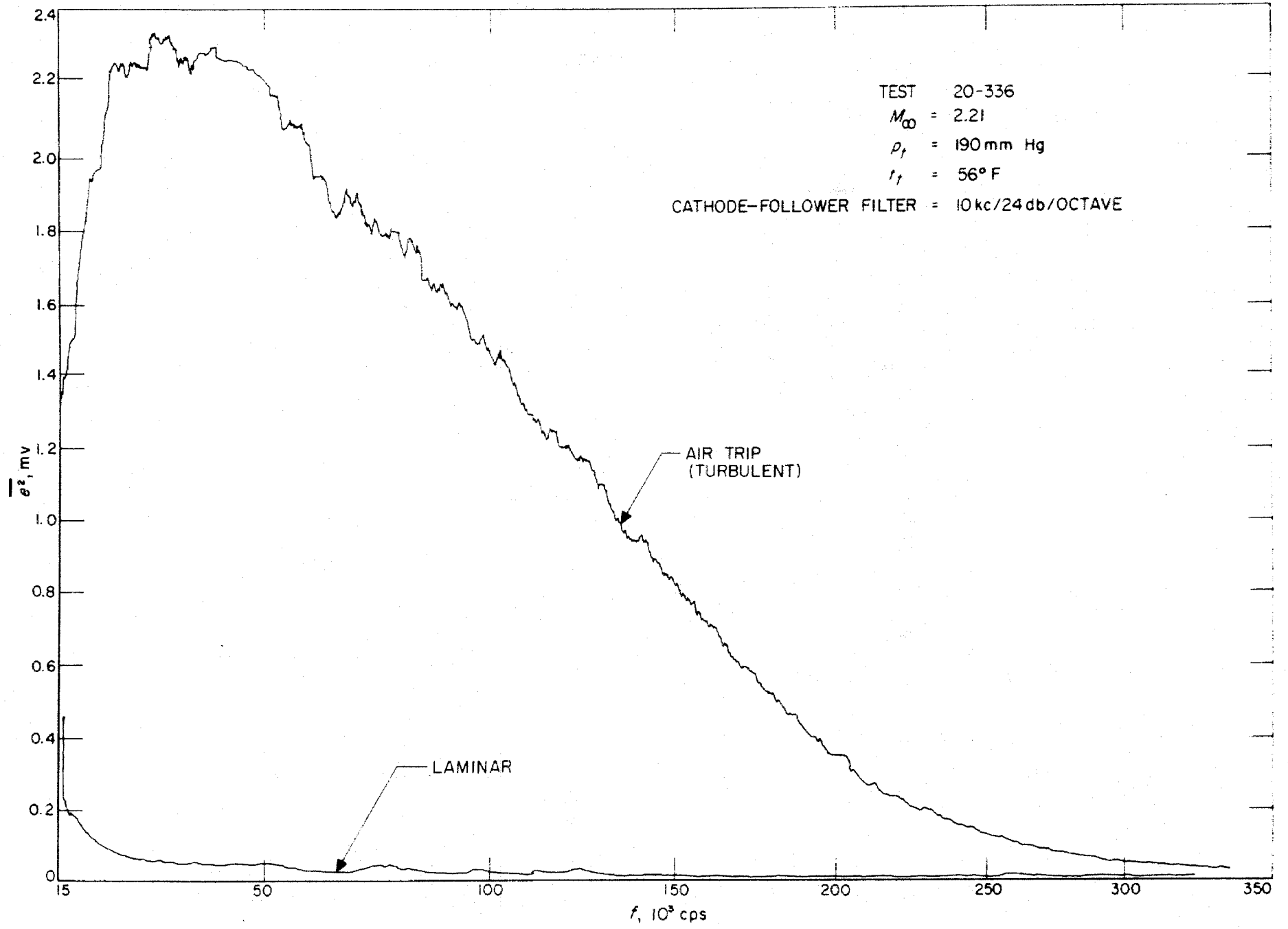
TEST 20-336
M_∞ = 2.21
p_t = 190 mm Hg
t_t = 56° F
CATHODE-FOLLOWER FILTER = 10 kc/24 db/OCTAVE
AIR TRIP (TURBULENT)
LAMINAR
$\overline{e^2}$, mv
f, 10^3 cps
0
0.2
0.4
0.6
0.8
1.0
1.2
1.4
1.6
1.8
2.0
2.2
2.4
15
50
100
150
200
250
300
350

Fig 12

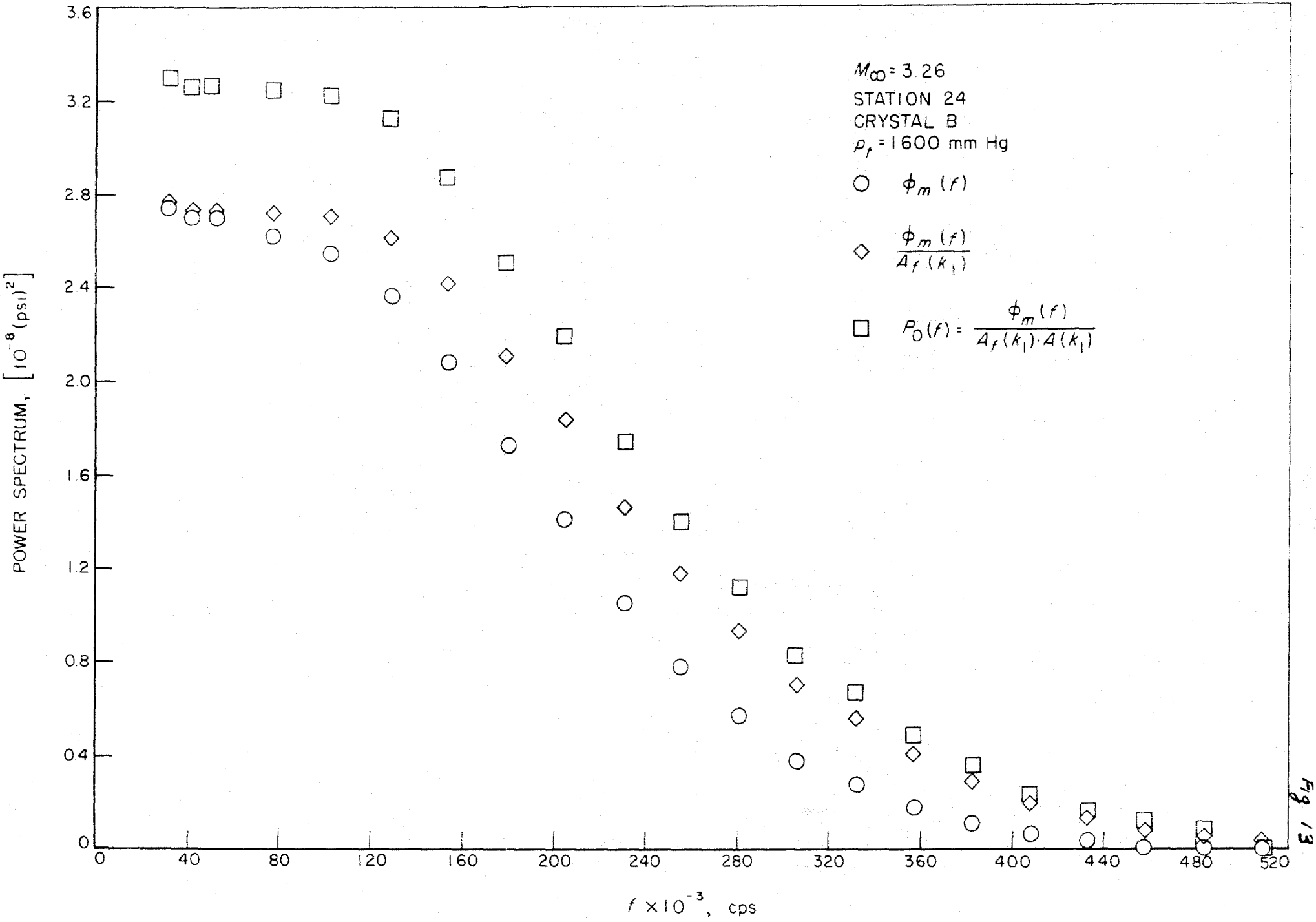
$M_\infty = 3.26$
STATION 24
CRYSTAL B
$p_t = 1600$ mm Hg
$\phi_m(f)$
$\frac{\phi_m(f)}{A_f(k_1)}$
$P_0(f) = \frac{\phi_m(f)}{A_f(k_1) \cdot A(k_1)}$
POWER SPECTRUM, $[10^{-8}(psi)^2]$
$f \times 10^{-3}$, cps
0
0.4
0.8
1.2
1.6
2.0
2.4
2.8
3.2
3.6
0
40
80
120
160
200
240
280
320
360
400
440
480
520

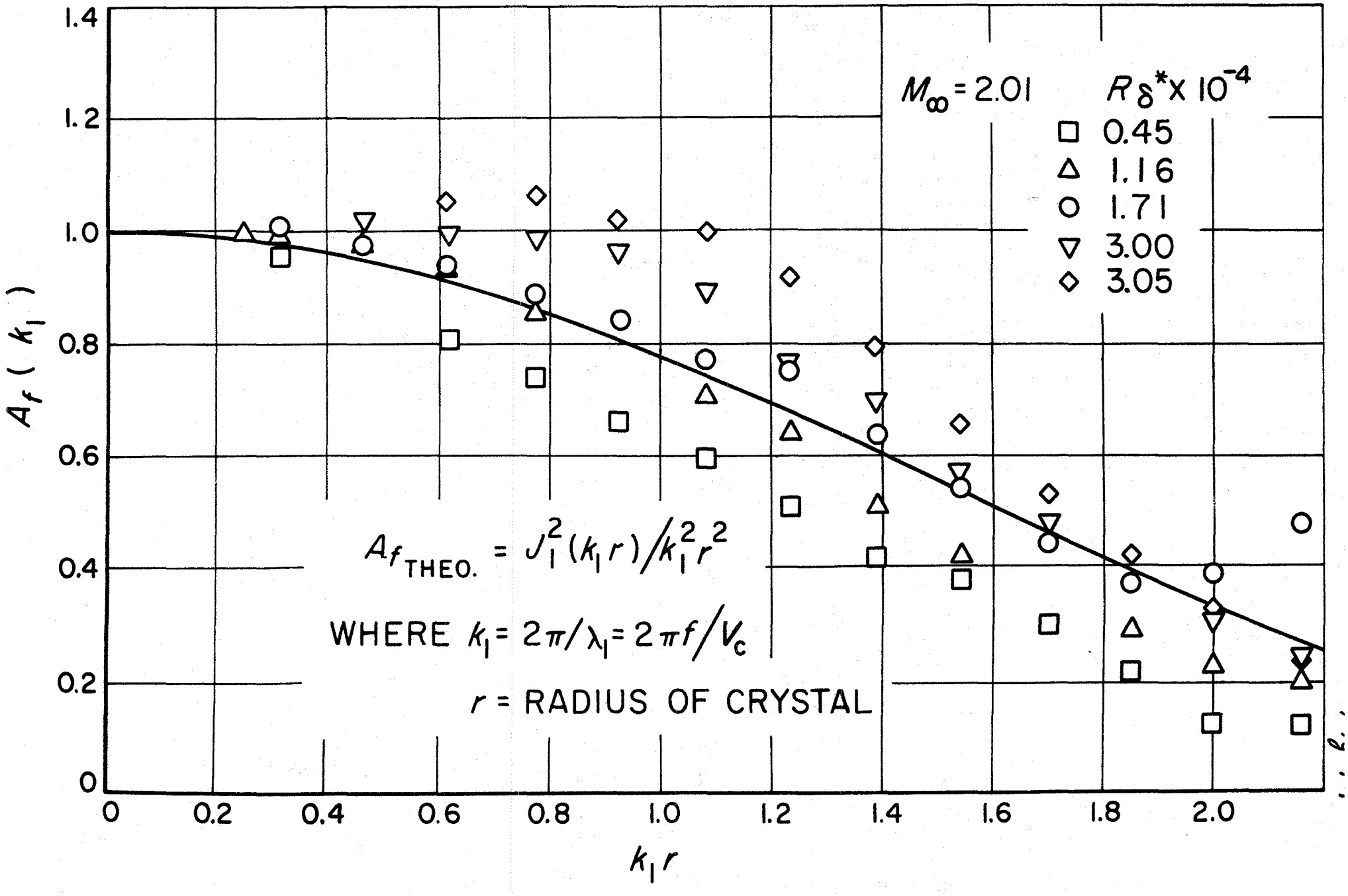
$M_\infty = 2.01$
$R\delta^* \times 10^{-4}$
0.45
1.16
1.71
3.00
3.05
$A_{f_{THEO.}} = J_1^2(k_1 r)/k_1^2 r^2$
WHERE $k_1 = 2\pi/\lambda_1 = 2\pi f/V_c$
r = RADIUS OF CRYSTAL
$A_f(k_1)$
$k_1 r$
0
0.2
0.4
0.6
0.8
1.0
1.2
1.4
1.6
1.8
2.0

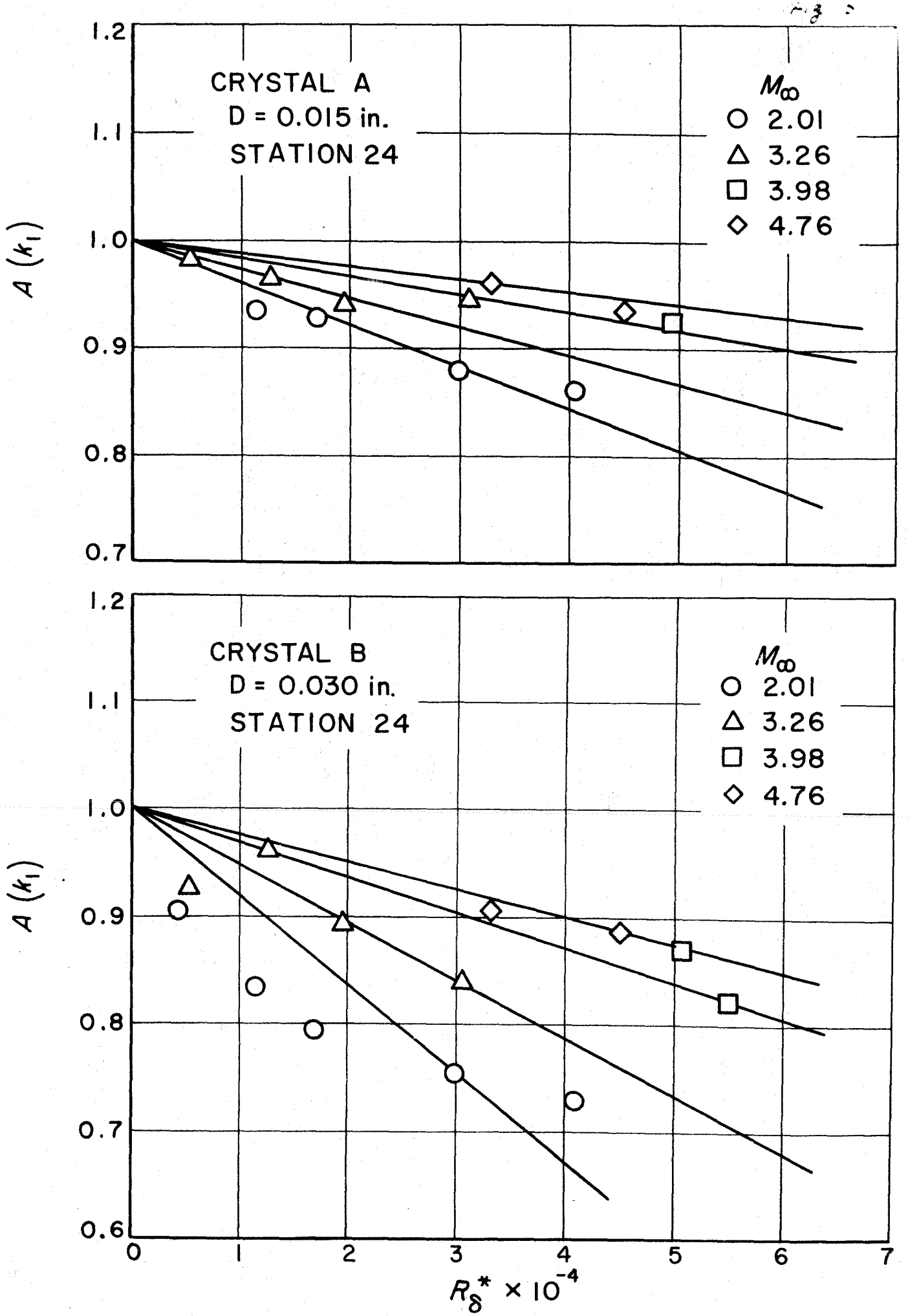
CRYSTAL A
D = 0.015 in.
STATION 24
M_∞
2.01
3.26
3.98
4.76
$A(k_1)$
1.2
1.1
1.0
0.9
0.8
0.7
CRYSTAL B
D = 0.030 in.
STATION 24
M_∞
2.01
3.26
3.98
4.76
$A(k_1)$
1.2
1.1
1.0
0.9
0.8
0.7
0.6
0
1
2
3
4
5
6
7
$R_\delta^* \times 10^{-4}$

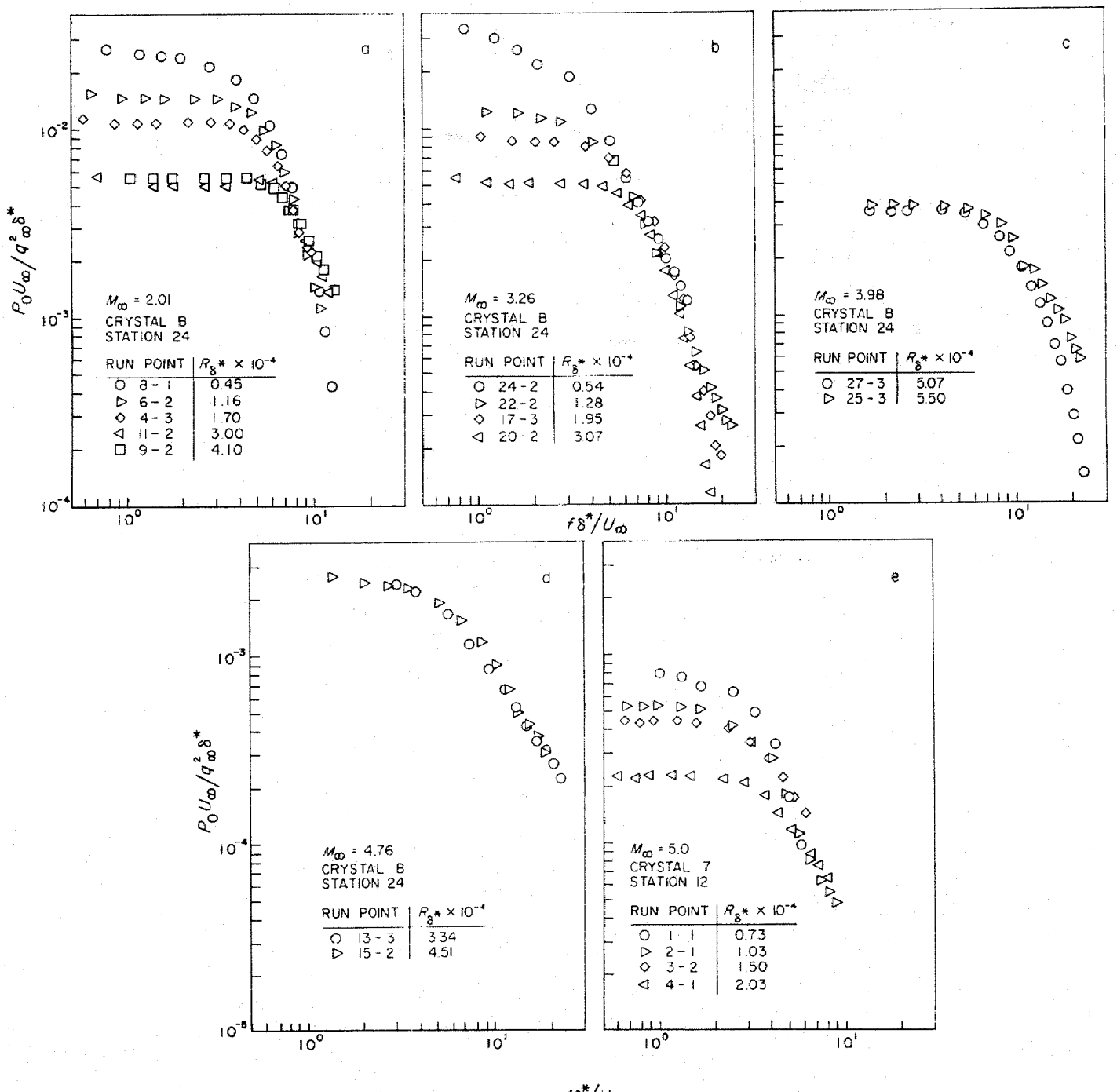
a
M_∞ = 2.01
CRYSTAL B
STATION 24
RUN POINT | $R_\delta^* \times 10^{-4}$
8-1 | 0.45
6-2 | 1.16
4-3 | 1.70
11-2 | 3.00
9-2 | 4.10
b
M_∞ = 3.26
CRYSTAL B
STATION 24
RUN POINT | $R_\delta^* \times 10^{-4}$
24-2 | 0.54
22-2 | 1.28
17-3 | 1.95
20-2 | 3.07
c
M_∞ = 3.98
CRYSTAL B
STATION 24
RUN POINT | $R_\delta^* \times 10^{-4}$
27-3 | 5.07
25-3 | 5.50
d
M_∞ = 4.76
CRYSTAL B
STATION 24
RUN POINT | $R_\delta^* \times 10^{-4}$
13-3 | 3.34
15-2 | 4.51
e
M_∞ = 5.0
CRYSTAL 7
STATION 12
RUN POINT | $R_\delta^* \times 10^{-4}$
1-1 | 0.73
2-1 | 1.03
3-2 | 1.50
4-1 | 2.03
$P_0 U_\infty / q^2_\infty \delta^*$
$f\delta^*/U_\infty$

Fig 16a

Fig 16b

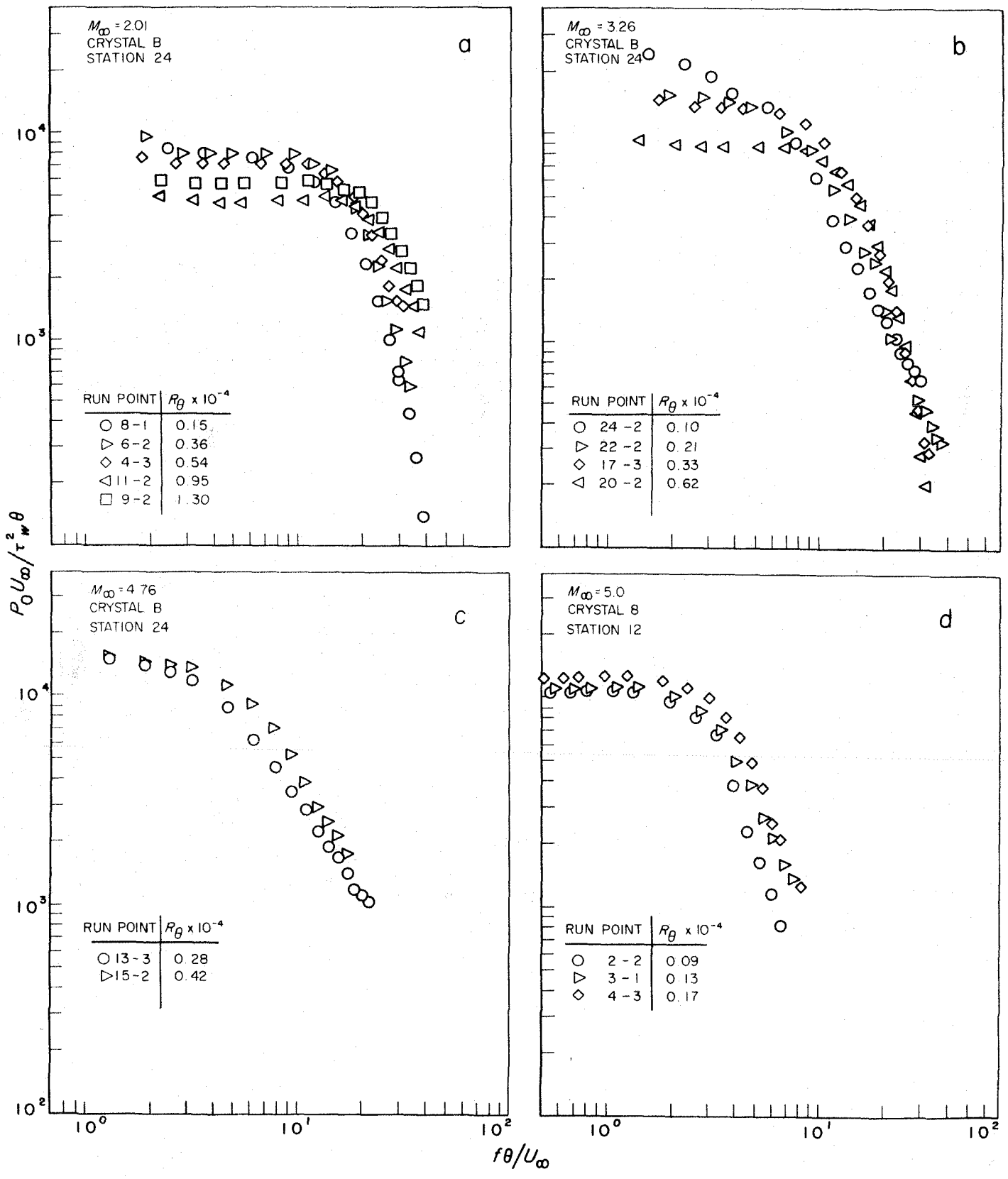
M_∞ = 2.01
CRYSTAL B
STATION 24
a
RUN POINT | $R_\theta \times 10^{-4}$
8-1 | 0.15
6-2 | 0.36
4-3 | 0.54
11-2 | 0.95
9-2 | 1.30
M_∞ = 3.26
CRYSTAL B
STATION 24
b
RUN POINT | $R_\theta \times 10^{-4}$
24-2 | 0.10
22-2 | 0.21
17-3 | 0.33
20-2 | 0.62
M_∞ = 4.76
CRYSTAL B
STATION 24
c
RUN POINT | $R_\theta \times 10^{-4}$
13-3 | 0.28
15-2 | 0.42
M_∞ = 5.0
CRYSTAL 8
STATION 12
d
RUN POINT | $R_\theta \times 10^{-4}$
2-2 | 0.09
3-1 | 0.13
4-3 | 0.17
$P_0 U_\infty / \tau_w^2 \theta$
$f\theta/U_\infty$
10^2
10^3
10^4
10^0
10^1
10^2

Fig 17a

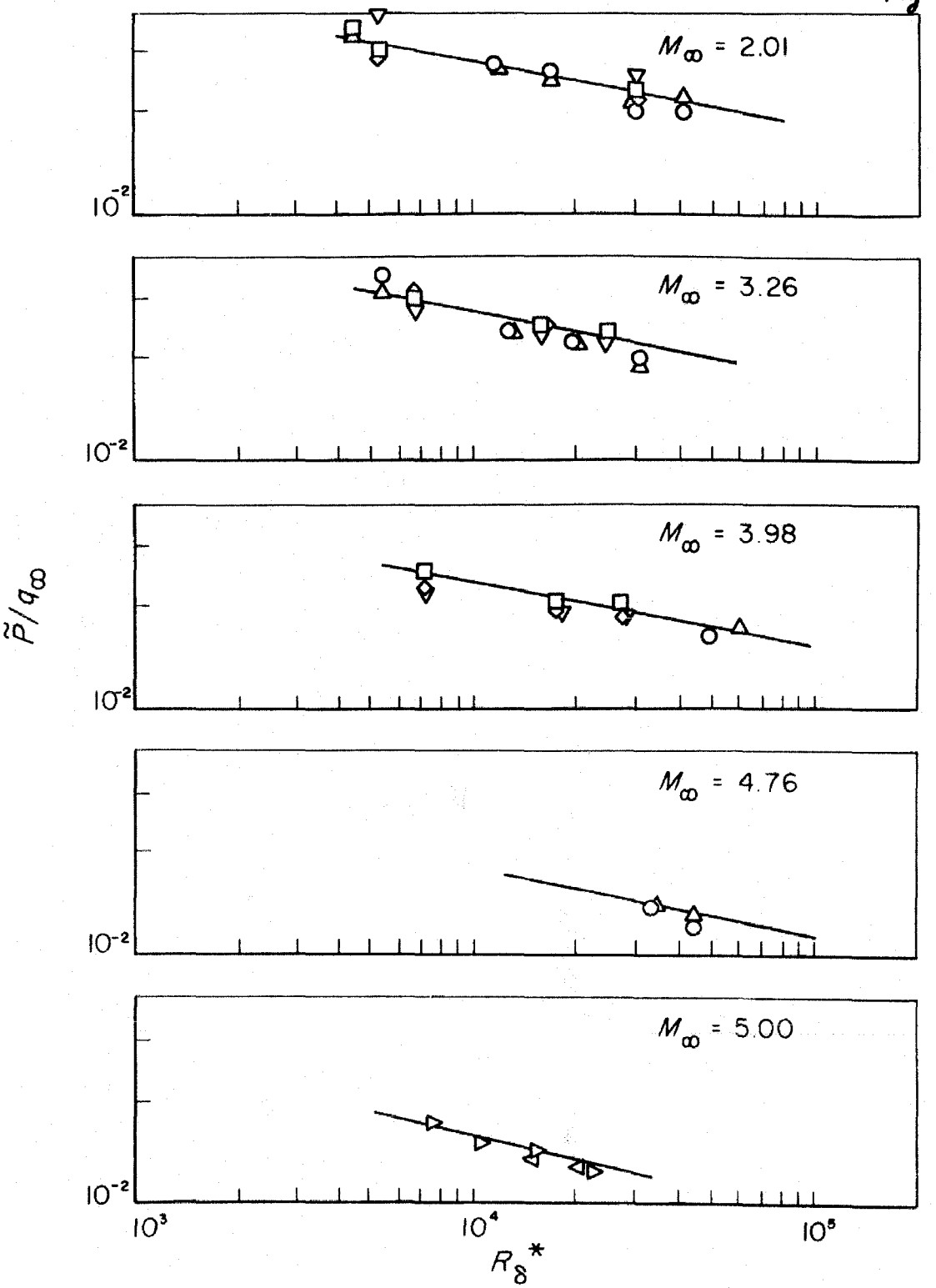

SYMBOL	CRYSTAL	D, in.	STATION
○	A	0.015	24
△	B	0.03	24
□	4	0.015	13
◇	5	0.015	13
▽	6	0.03	13
▷	7	0.03	13
◁	8	0.03	13

Fig 17 b

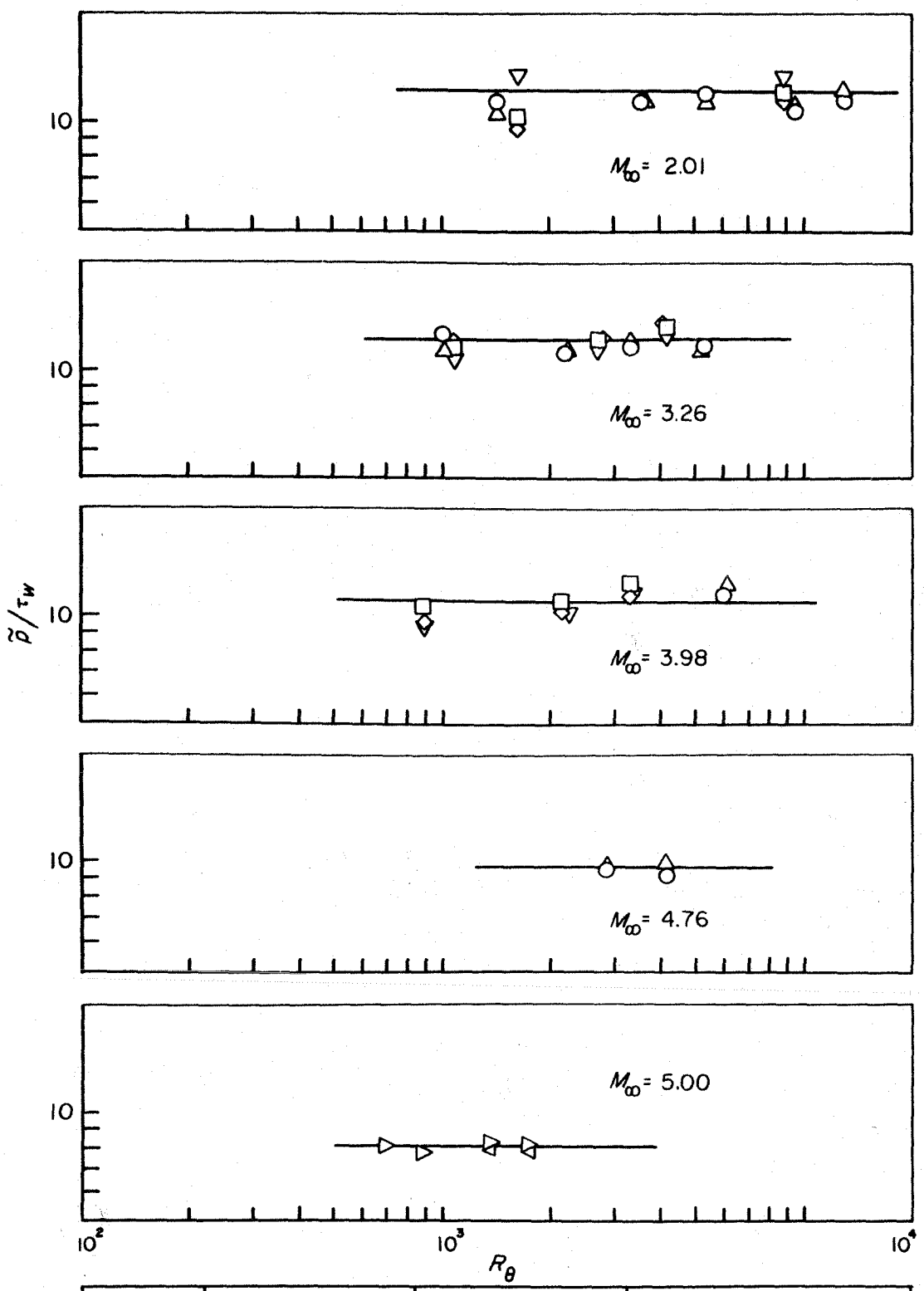

	CRYSTAL	D, in.	STATION
○	A	0.015	24
△	B	0.030	24
◇	4	0.015	13
□	5	0.015	13
▽	6	0.030	13
▷	7	0.030	13
◁	8	0.030	13

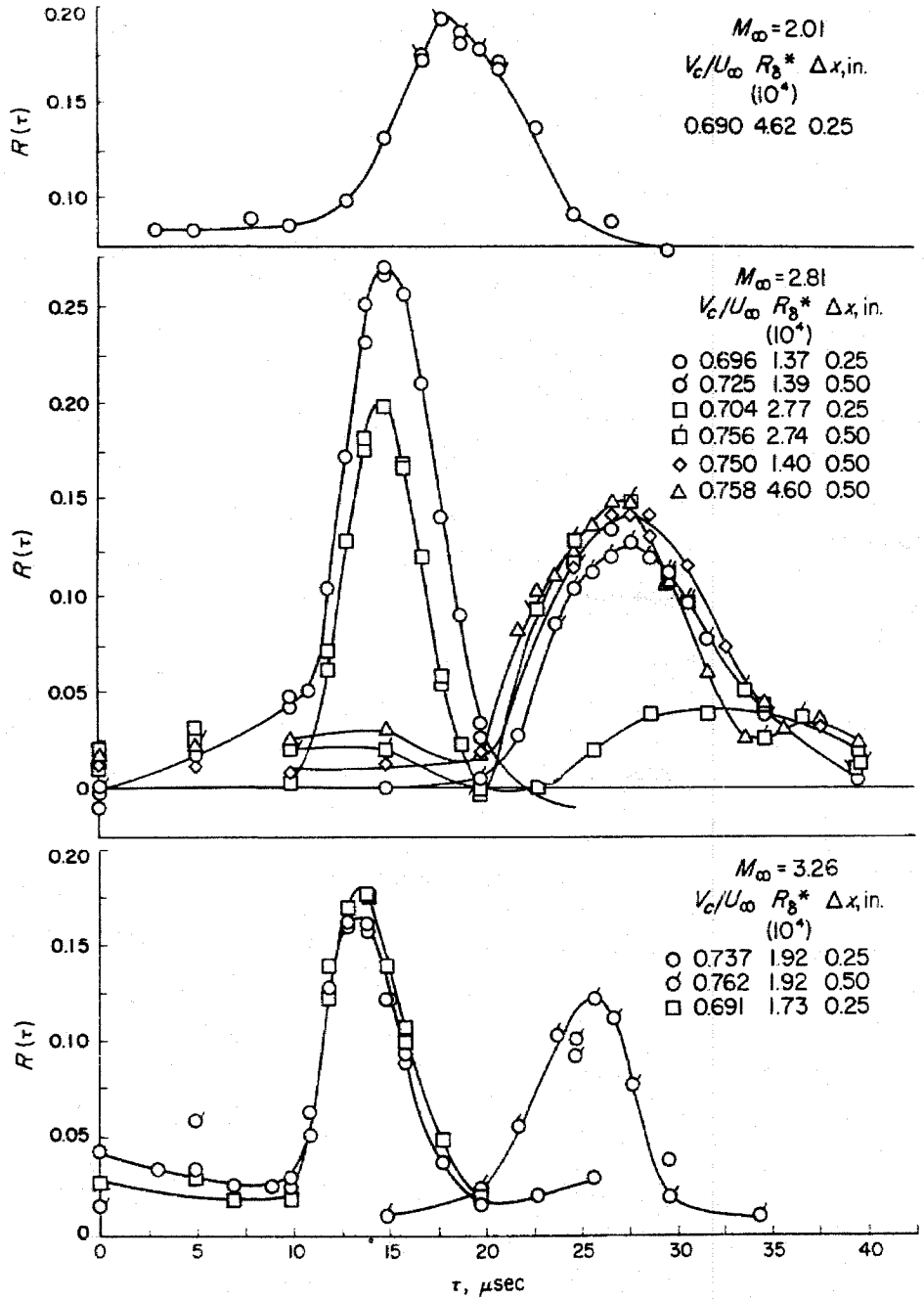
$M_\infty = 2.01$
V_c/U_∞ R_δ^* Δx, in.
(10^4)
0.690 4.62 0.25
$M_\infty = 2.81$
V_c/U_∞ R_δ^* Δx, in.
(10^4)
0.696 1.37 0.25
0.725 1.39 0.50
0.704 2.77 0.25
0.756 2.74 0.50
0.750 1.40 0.50
0.758 4.60 0.50
$M_\infty = 3.26$
V_c/U_∞ R_δ^* Δx, in.
(10^4)
0.737 1.92 0.25
0.762 1.92 0.50
0.691 1.73 0.25
$R(\tau)$
τ, μsec

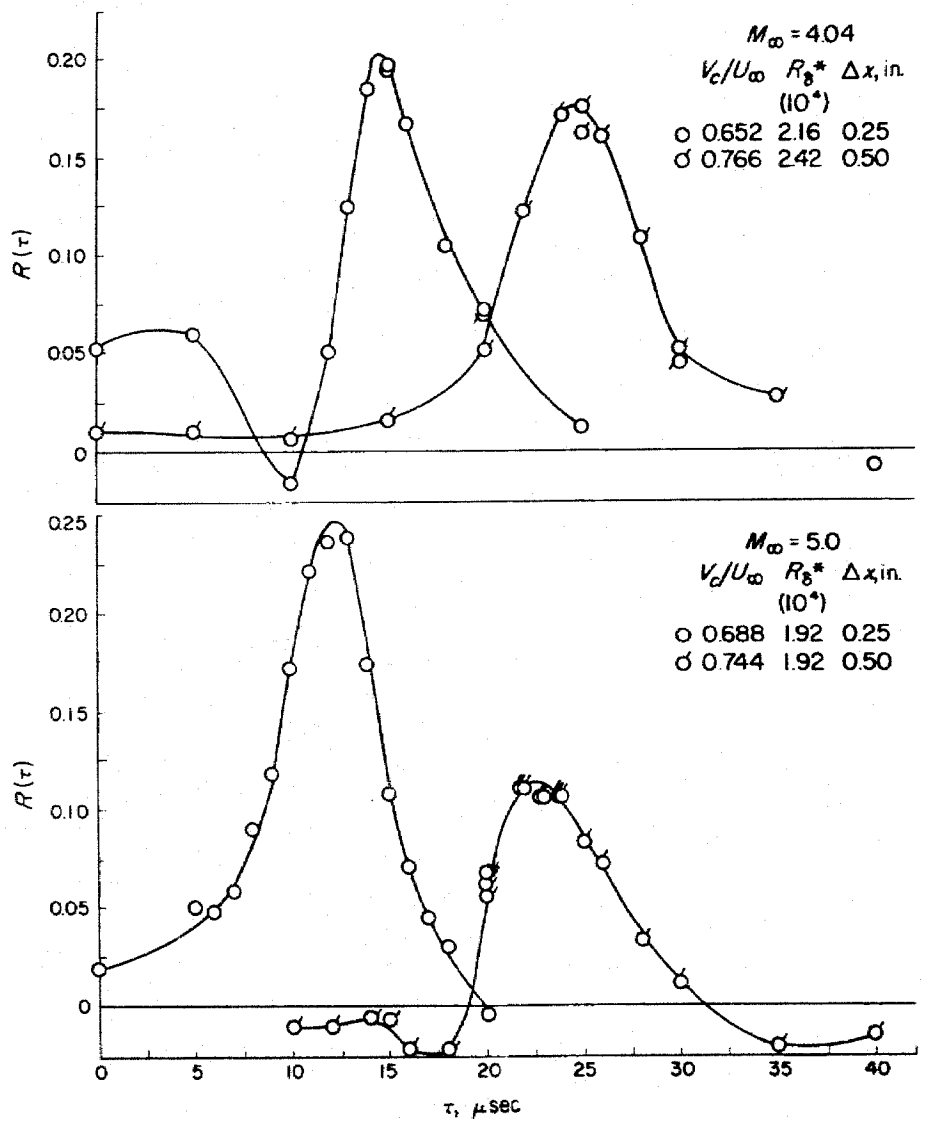
$M_\infty = 4.04$
V_c/U_∞ R_δ^* Δx, in.
(10^4)
0.652 2.16 0.25
0.766 2.42 0.50
$M_\infty = 5.0$
V_c/U_∞ R_δ^* Δx, in.
(10^4)
0.688 1.92 0.25
0.744 1.92 0.50
$R(\tau)$
τ, μsec

Fig 18

Fig 19a

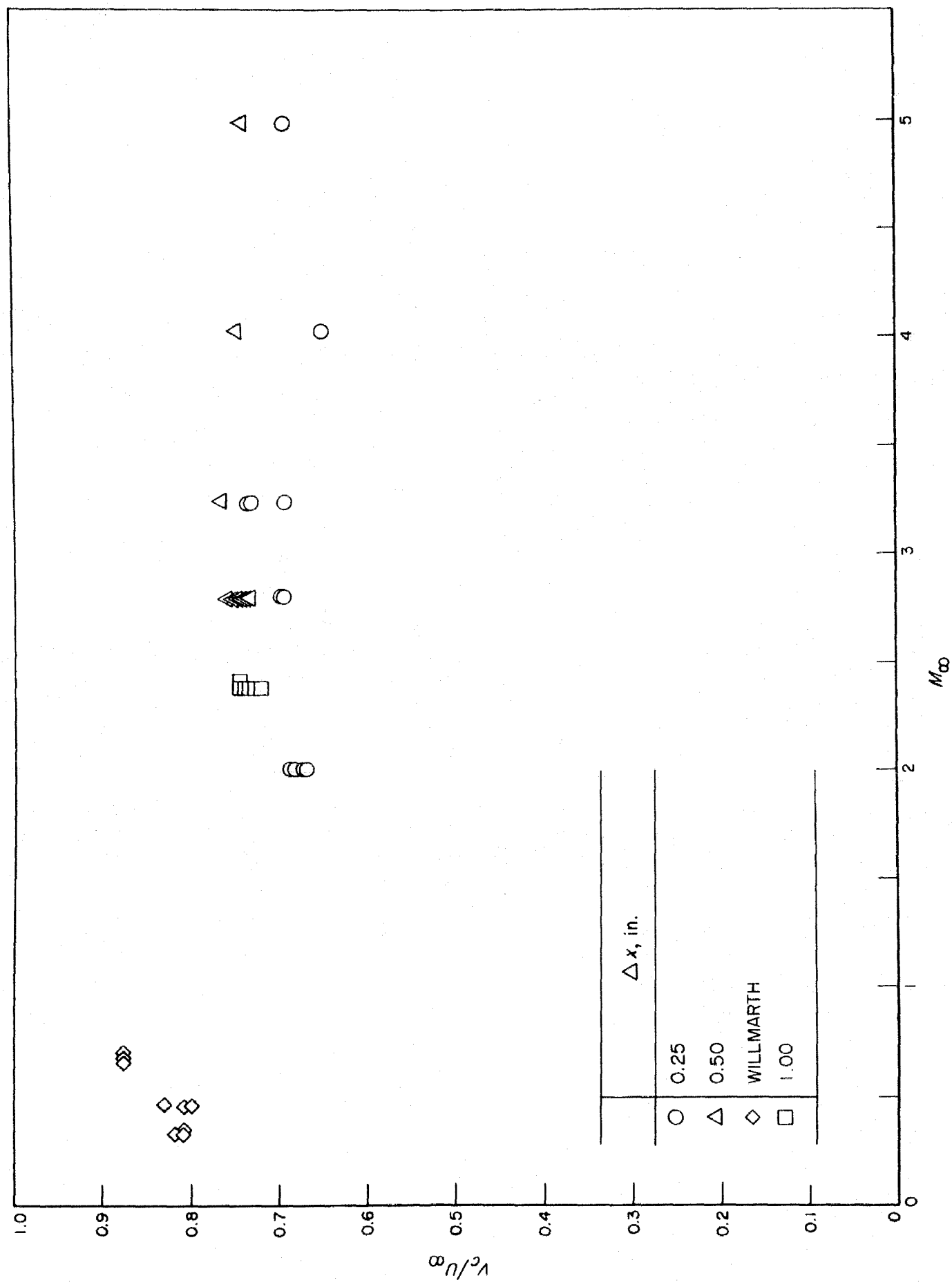
v_c/U_∞
M_∞
0
0.1
0.2
0.3
0.4
0.5
0.6
0.7
0.8
0.9
1.0
1
2
3
4
5
Δx, in.
0.25
0.50
WILLMARTH
1.00

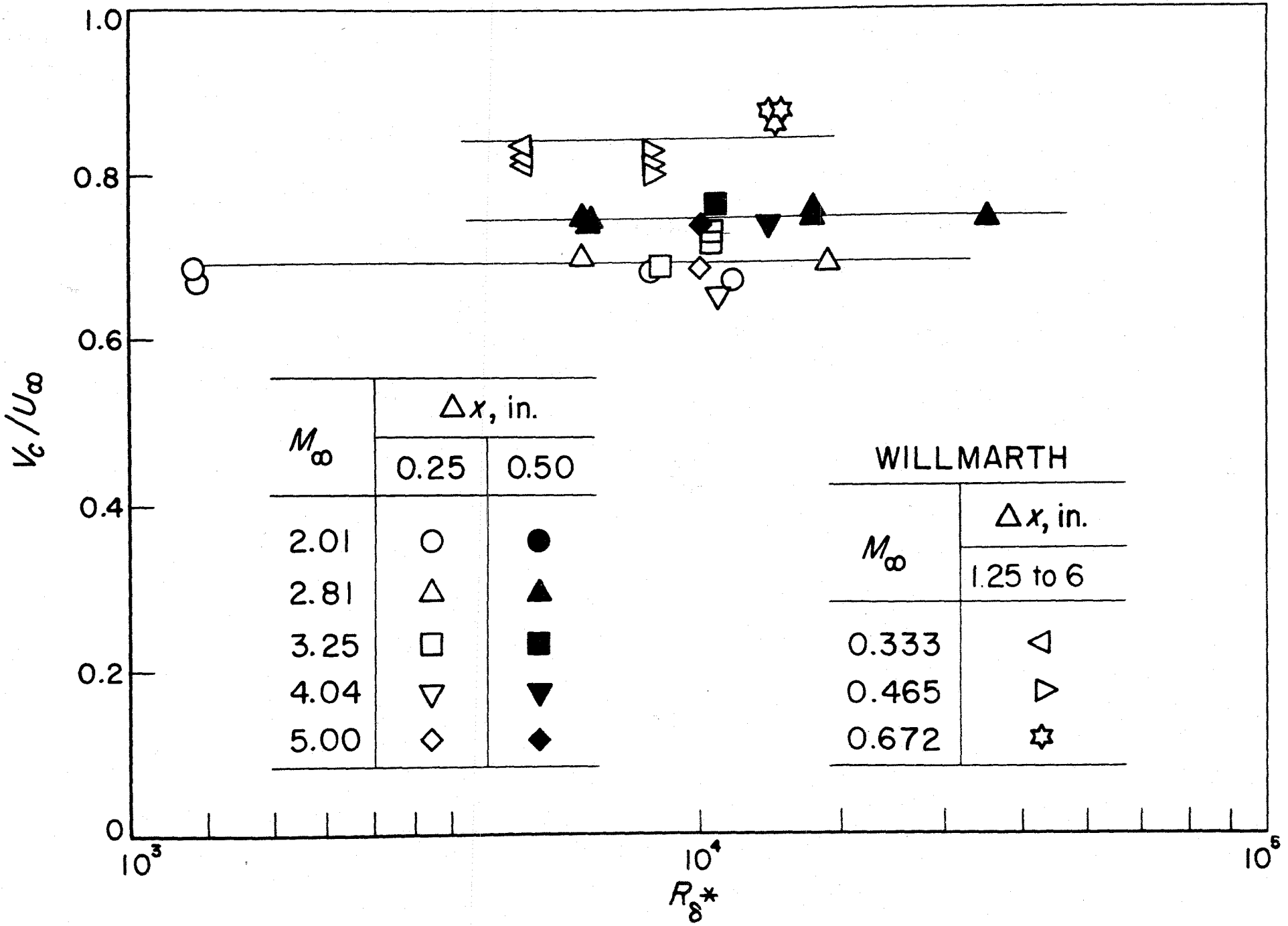
1.0
0.8
0.6
0.4
0.2
0
V_c/U_∞
10^3
10^4
10^5
R_δ^*
M_∞
Δx, in.
0.25
0.50
2.01
2.81
3.25
4.04
5.00
WILLMARTH
M_∞
Δx, in.
1.25 to 6
0.333
0.465
0.672

Fig 20a

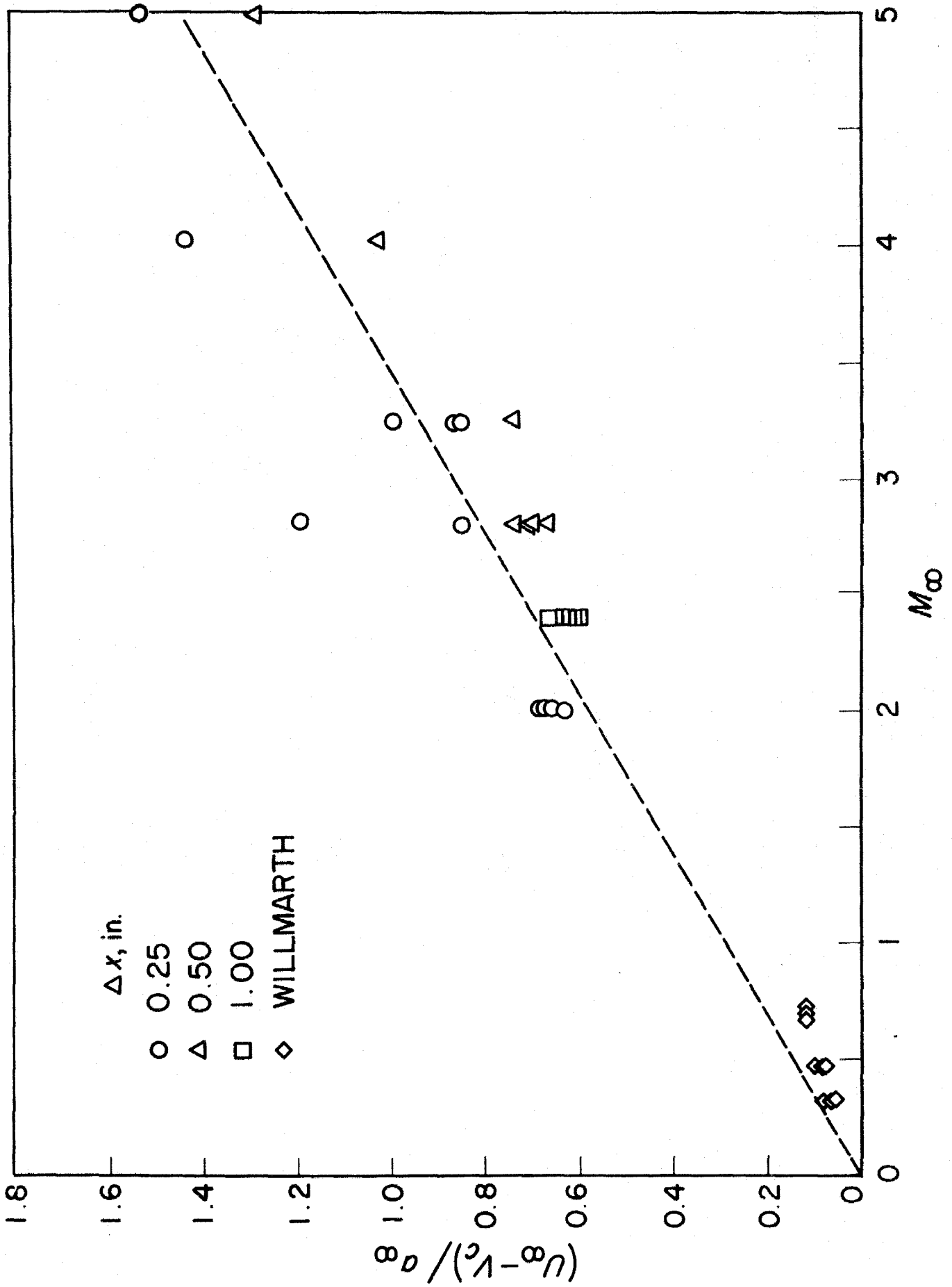
$(U_\infty - V_c)/a_\infty$
M_∞
0
0.2
0.4
0.6
0.8
1.0
1.2
1.4
1.6
1.8
0
1
2
3
4
5
Δx, in.
0.25
0.50
1.00
WILLMARTH

Fig 20 b

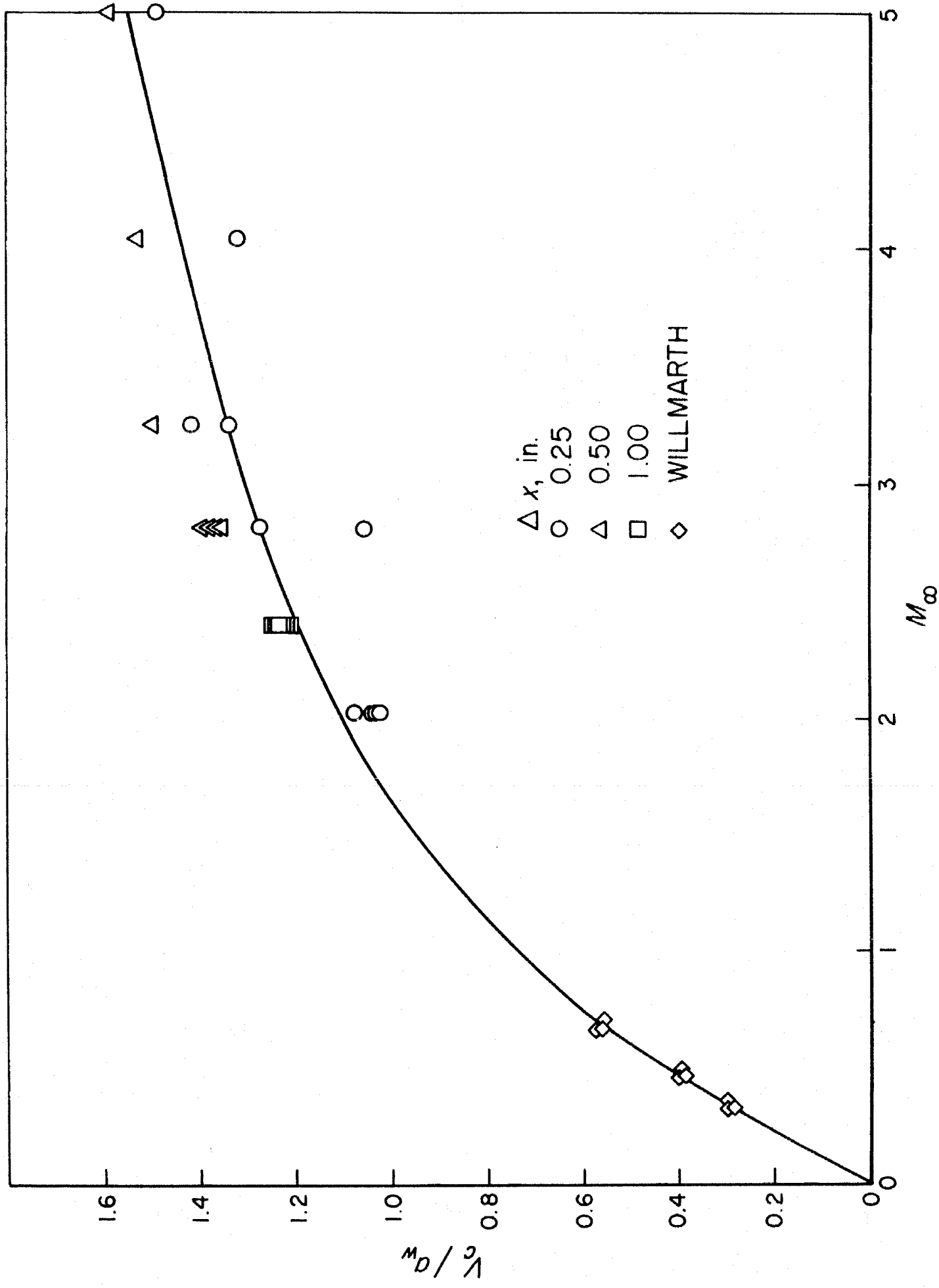
M_{∞}
u_D / a_c
0
1
2
3
4
5
0.2
0.4
0.6
0.8
1.0
1.2
1.4
1.6
Δ x, in.
0.25
0.50
1.00
WILLMARTH